Deformable Image Registration with Hyperelastic Warping

Alexander I. Veress [1], *Nikhil Phatak* [1], *Jeffrey A. Weiss* [1]

1. Introduction

The extraction of quantitative information regarding growth and deformation from series of image data is of significant importance in many fields of science and medicine. Imaging techniques such as MRI, CT and ultrasound provide a means to examine the morphology and in some cases metabolism of tissues. The registration of this image data between different time points after external loading, treatment, disease or other pathologies is performed using methods known as deformable image registration.

The goal of deformable image registration is to find a transformation that best aligns the features of a "template" and "target" image (Figure 1). In the ideal case, the quantity and quality of the image texture present in the template and target

[1] Department of Bioengineering, University of Utah, Salt Lake City, UT

images, as well as the similarity in underlying anatomical structure, would yield a unique "best" transformation. In real problems, however, this is not the case. Deformable image registration is most often ill-posed in the sense of Hadamard [1-3]. No perfect transformation exists, and the solution depends on the choice of the cost function and associate solution methods.

Deformable image registration grew primarily out of the pattern recognition field where significant effort has been devoted to the representation of image ensembles (e.g., [4-13]). The approaches that are used are usually classified as either model-based or pixel-based. Model-based approaches typically require some segmentation of a surface in the 3D image dataset. This surface is then warped into alignment with features in the target image. The pixel-based approaches do not in general require a segmentation, but rather deform pixels or some sampling of the pixels.

Most methods for deformable registration incorporate a cost function so that the overall energy function to be minimized consists of one term based on the image data itself and a second term that serves to regularize the problem. The choice of this cost function can have a significant effect on the results of image registration. The dependence is most significant in regions of the template model where image texture is sparse or conflicting. In these regions, the registration solution is computed based on minimizing the

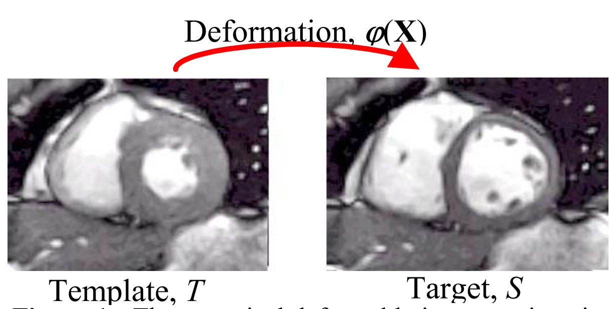

Figure 1: The canonical deformable image registration problem involves the determination of the deformation map that will align a template image with a target image. In this case, the data are MR images of a heart at different times during the cardiac cycle.

deformation potential (Bayesian prior probability) portion of the particular registration cost functional [14]. A common approach is to use an analogy to a physical material by treating the original template image as an elastic sheet [12, 13, 15, 16] or a viscous fluid [17]. In general, these approaches benefit from the fact that the mapping from template to target is guaranteed to be one-to-one on the basis of the fundamentals of deformations as defined in continuum mechanics. However, the particular kinematic and constitutive assumptions can over-constrain the solution. As an example, use of the theory of linearized elasticity results in the over-penalization of large rotations, thus limiting the ability to achieve a good registration.

The objective of this chapter is to describe the theory and application of a method termed hyperelastic Warping [16, 18-22] to problems in deformable image registration. The method is based on the principles of nonlinear solid mechanics to allow objective tracking of large deformations and rotations and the concomitant determination of stresses within the deforming body. The approach may be applied to physical deformations that arise in solid and fluid mechanics as well as to non-physical deformations such as the inter- and intra-subject registration of image data. For the physical deformation case, the goal is to quantify the kinematics and the kinetics of the deformations. In the non-physical case, only the kinematics of the deformations are sought.

2. Hyperelastic Warping

The standard notation and symbols of modern continuum mechanics are employed in the following presentation [23-25]. In particular, direct notation is used, with boldface italics for vector and tensor fields. The outer product is denoted with "⊗", a matrix inner product is denoted with ":", and a matrix-vector product is denoted with "·". Index notation is incorporated for quantities that cannot be readily written in with direct notation. The condensed Voigt notation typically employed in finite element (FE) analysis is utilized as needed[1].

2.1. Finite Deformation Theory

A Lagrangian reference frame is assumed in the following presentation, and thus the kinematics of material points corresponding to the template image are tracked with respect to their original positions. However, it should be noted that the approach could be adapted readily to an Eulerian framework. The template and target images are assumed to have spatially varying scalar intensity fields defined with respect to the reference configuration and denoted by T and S, respectively. The deformation map is denoted $\boldsymbol{\varphi}(\boldsymbol{X}) = \boldsymbol{x} = \boldsymbol{X} + \boldsymbol{u}(\boldsymbol{X})$ where $\boldsymbol{x}$ are the current (deformed) coordinates corresponding to $\boldsymbol{X}$ and $\boldsymbol{u}(\boldsymbol{X})$ is the displacement field. $\boldsymbol{F}$ is the deformation gradient [26]:

$$\boldsymbol{F}(\boldsymbol{X}) = \frac{\partial \boldsymbol{\varphi}(\boldsymbol{X})}{\partial \boldsymbol{X}}. \tag{1}$$

The local change in density is directly related to the deformation gradient through the Jacobian, $J := \det(\boldsymbol{F}) = \rho_0/\rho$, where det($\boldsymbol{F}$) is the determinant of the deformation gradient, ρ_0 is the density in the reference configuration and ρ is the density in the deformed configuration. At this point, it is assumed that T and S have a general dependence on position in the reference configuration $\boldsymbol{X}$ and the deformation map $\boldsymbol{\varphi}(\boldsymbol{X})$.

The positive definite, symmetric right and left Cauchy-Green deformation tensors are, respectively,

$$\boldsymbol{C} = \boldsymbol{F}^T\boldsymbol{F} = \boldsymbol{U}^2 \text{ and } \boldsymbol{B} = \boldsymbol{F}\boldsymbol{F}^T = \boldsymbol{U}^2 . \tag{2}$$

The Jacobian J is defined as:

$$J := \det \boldsymbol{F} = \frac{\rho_0}{\rho} . \tag{3}$$

2.2. Variational Framework

Most deformable image registration methods can be posed as the minimization of an energy functional E that consists of two terms. This can be defined with respect to the reference or current (deformed) configuration as:

$$\begin{aligned} E(\boldsymbol{X},\boldsymbol{\varphi}) &= \int_{\boldsymbol{\beta}_0} W(\boldsymbol{X},\boldsymbol{\varphi})\,dV - \int_{\boldsymbol{\beta}_0} U\big(T(\boldsymbol{X},\boldsymbol{\varphi}),S(\boldsymbol{X},\boldsymbol{\varphi})\big)\,dV \\ &= \int_{\boldsymbol{\beta}} W(\boldsymbol{X},\boldsymbol{\varphi})\frac{dv}{J} - \int_{\boldsymbol{\beta}} U\big(T(\boldsymbol{X},\boldsymbol{\varphi}),S(\boldsymbol{X},\boldsymbol{\varphi})\big)\frac{dv}{J} \end{aligned} . \tag{4}$$

Here, W is an energy term that provides regularization and/or some type of constraint on the deformation map (e.g., one-to-one mapping or no negative volumes admitted), while U represents an energy that depends on the image data in the template and target images. β_0 and β represent the volumes of integration in the reference and current configurations, respectively.

The Euler-Lagrange equations are obtained by taking the first variation of $E(\boldsymbol{X},\boldsymbol{\varphi})$ with respect to the deformation $\boldsymbol{\varphi}$. This can be thought of as a "virtual displacement" – a small variation in the current coordinates $\boldsymbol{x}$, denoted $\varepsilon\boldsymbol{\eta}$. Here ε is an infinitesimal scalar. The first variation of the first energy term in (4) defines the forces per unit volume that arise from the regularization. The second energy term in (4) gives rise to an image-based force term. The first variation of (4) with respect to the deformation $\boldsymbol{\varphi}(\boldsymbol{X})$ in direction $\boldsymbol{\eta}$ is denoted:

$$G(\boldsymbol{\varphi},\boldsymbol{\eta}) := DE(\boldsymbol{\varphi})\cdot\boldsymbol{\eta} = \int_{\beta} DW(\boldsymbol{X},\boldsymbol{\varphi})\cdot\boldsymbol{\eta}\,\frac{dv}{J} + \int_{\beta} DU\big(T(\boldsymbol{X},\boldsymbol{\varphi}),S(\boldsymbol{X},\boldsymbol{\varphi})\big)\cdot\boldsymbol{\eta}\,\frac{dv}{J} = 0\,. \quad (5)$$

The variations are calculated by taking the Gateaux derivative [25] of the functional U evaluated at $\boldsymbol{\varphi}+\varepsilon\boldsymbol{\eta}$ with respect to ε and then letting $\varepsilon \to 0$. For general forms of W and U,

$$G(\boldsymbol{\varphi},\boldsymbol{\eta}) = \int_{\beta} \frac{\partial W}{\partial \boldsymbol{\varphi}}\cdot\boldsymbol{\eta}\,\frac{dv}{J} + \int_{\beta} \frac{\partial U}{\partial \boldsymbol{\varphi}}\cdot\boldsymbol{\eta}\,\frac{dv}{J} = 0\,. \quad (6)$$

2.3. Linearization

Equation (6) is highly nonlinear and thus an incremental-iterative solution method is necessary to obtain the configuration $\boldsymbol{\varphi}$ that satisfies the equation [27]. The most common approach is based on linearization of the equations and an iterative solution using Newton's method or some variant. Assuming that the solution at a configuration $\boldsymbol{\varphi}^*$ is known, a solution is sought at some small increment

$\boldsymbol{\varphi}^* + \Delta\boldsymbol{u}$. Here again, $\Delta\boldsymbol{u}$ is a variation in the configuration or a virtual displacement. The linearization of (6) at $\boldsymbol{\varphi}^*$ in the direction $\Delta\boldsymbol{u}$ is:

$$L_{\varphi^*} G = G\left(\boldsymbol{\varphi}^*, \boldsymbol{\eta}\right) + DG\left(\boldsymbol{\varphi}^*, \boldsymbol{\eta}\right) \cdot \Delta\boldsymbol{u} = \int_{\beta} \boldsymbol{\eta} \cdot \left(\frac{\partial W}{\partial \boldsymbol{\varphi}} + \frac{\partial U}{\partial \boldsymbol{\varphi}} \right) \frac{dv}{J} + \int_{\beta} \boldsymbol{\eta} \cdot \left(\mathbf{D} + \mathbf{k} \right) \cdot \Delta\boldsymbol{u} \frac{dv}{J}, \quad (7)$$

where $\mathbf{k} := \dfrac{\partial^2 U}{\partial \boldsymbol{\varphi} \partial \boldsymbol{\varphi}}$ is the *image stiffness* and $\mathbf{D} := \dfrac{\partial^2 W}{\partial \boldsymbol{\varphi} \partial \boldsymbol{\varphi}}$ is the *regularization stiffness*. These 2nd derivative terms (Hessians) describe how small perturbations of the current configuration affect the contributions of *W* and *U* to the overall energy of the system.

2.4. Particular Forms for *W* and *U* – Hyperelastic Warping

In hyperelastic Warping, a physical representation of the template image is deformed into alignment with the target image which remains fixed in the reference configuration. The scalar intensity field of the template, *T*, is not changed directly by the deformation, and thus it is represented as $T(\boldsymbol{X})$. Since the values of *S* at material points associated with the deforming template change as the template deforms with respect to the target, it is written as $S(\boldsymbol{\varphi})$. The formulation uses a Gaussian sensor model to describe the image energy density functional:

$$U\left(\boldsymbol{X}, \boldsymbol{\varphi}\right) = \frac{\lambda}{2}\left(T\left(\boldsymbol{X}\right) - S\left(\boldsymbol{\varphi}\right)\right)^2. \quad (8)$$

λ is a penalty parameter [28] that enforces the alignment of the template model with the target image data. As $\lambda \to \infty$, $\left(T\left(\boldsymbol{X}\right) - S\left(\boldsymbol{\varphi}\right)\right)^2 \to 0$, and the image energy converges to a finite value.

Hyperelastic Warping assumes that W is the standard strain energy density function from continuum mechanics that defines the material constitutive behavior. It depends on the right deformation tensor $\boldsymbol{C}$. The right deformation tensor is independent of rotation and thus hyperelasticity provides an objective (invariant under rotation) constitutive framework, in contrast to linearized elasticity (see below, [29]). With these specific assumptions, equation (4) takes the form:

$$E = \int_{\beta} W\left(\boldsymbol{X},\boldsymbol{C}\right)\frac{dv}{J} - \int_{\beta} U\left(T\left(\boldsymbol{X}\right), S\left(\boldsymbol{\varphi}\right)\right)\frac{dv}{J} \tag{9}$$

The first variation of the first term in (9) yields the standard weak from of the momentum equations for nonlinear solid mechanics (see, e.g., [25]). The first variation of the functional U in (8) with respect to the deformation $\boldsymbol{\varphi}(\boldsymbol{X})$ in direction $\boldsymbol{\eta}$ gives rise to the image-based force term:

$$\begin{aligned} DU\left(\boldsymbol{\varphi}\right)\cdot\boldsymbol{\eta} &= D\left[\frac{\lambda}{2}\left(T\left(\boldsymbol{X}\right)-S\left(\boldsymbol{\varphi}\right)\right)^2\right]\cdot\boldsymbol{\eta} \\ &= \lambda\left[\left(T\left(\boldsymbol{X}\right)-S\left(\boldsymbol{\varphi}+\varepsilon\boldsymbol{\eta}\right)\right)\frac{\partial}{\partial\varepsilon}\left(T\left(\boldsymbol{X}\right)-S\left(\boldsymbol{\varphi}+\varepsilon\boldsymbol{\eta}\right)\right)\right]_{\varepsilon\to 0} \end{aligned}. \tag{10}$$

Noting that

$$\left[\frac{\partial}{\partial\varepsilon}\left(T\left(\boldsymbol{X}\right)-S\left(\boldsymbol{\varphi}+\varepsilon\boldsymbol{\eta}\right)\right)\right]_{\varepsilon\to 0} = \left[-\frac{\partial S\left(\boldsymbol{\varphi}+\varepsilon\boldsymbol{\eta}\right)}{\partial\left(\boldsymbol{\varphi}+\varepsilon\boldsymbol{\eta}\right)}\cdot\frac{\partial\left(\boldsymbol{\varphi}+\varepsilon\boldsymbol{\eta}\right)}{\partial\varepsilon}\right]_{\varepsilon\to 0} = -\frac{\partial S\left(\boldsymbol{\varphi}\right)}{\partial\boldsymbol{\varphi}}\cdot\boldsymbol{\eta}, \tag{11}$$

equations (10) and (11) can be combined to yield:

$$DU\left(\boldsymbol{\varphi}\right)\cdot\boldsymbol{\eta} = -\lambda\left[\left(T\left(\boldsymbol{X}\right)-S\left(\boldsymbol{\varphi}\right)\right)\frac{\partial S\left(\boldsymbol{\varphi}\right)}{\partial\boldsymbol{\varphi}}\cdot\boldsymbol{\eta}\right]. \tag{12}$$

This term drives the deformation of the template based on the pointwise difference in the image intensities and the gradient of the target intensity evaluated at material points associated with the template.

A similar computation for the mechanical strain energy term W leads to the weak form of the momentum equations (see, e.g., [24]):

$$G(\varphi,\eta) := DE(\varphi)\cdot\boldsymbol{\eta} = \int_\beta \boldsymbol{\sigma} : \nabla\boldsymbol{\eta}\, dv - \int_\beta \lambda \left[(T-S)\frac{\partial S}{\partial \boldsymbol{\varphi}}\cdot\boldsymbol{\eta} \right] \frac{dv}{J} = 0\,. \quad (13)$$

Here, $\boldsymbol{\sigma}$ is the 2nd order symmetric Cauchy stress tensor,

$$\boldsymbol{\sigma} = \frac{1}{J}\boldsymbol{F}\frac{\partial W}{\partial \boldsymbol{C}}\boldsymbol{F}^T \quad . \quad (14)$$

Thus, the forces applied to the physical model of the deforming template due to the differences in the image data are opposed by internal forces that arise from the deformation of the material through the constitutive model. The particular form of W depends on the material and its symmetry (i.e., isotropic, transversely isotropic, etc.) [26, 30-33].

The linearization of equation (13) yields:

$$\begin{aligned} L_{\varphi^*} G(\varphi,\eta) &= \int_\beta \boldsymbol{\sigma} : \nabla\boldsymbol{\eta}\, dv - \int_\beta \lambda \left[(T-S)\frac{\partial S}{\partial \boldsymbol{\varphi}^*}\cdot\boldsymbol{\eta} \right] \frac{dv}{J} \\ &+ \int_\beta \nabla\boldsymbol{\eta} : \boldsymbol{\sigma} : \nabla(\Delta\boldsymbol{u})\, dv + \int_\beta \nabla^s\boldsymbol{\eta} : \mathbf{c} : \nabla^s(\Delta\boldsymbol{u})\, dv + \int_\beta \boldsymbol{\eta}\cdot\mathbf{k}\cdot\Delta\boldsymbol{u}\frac{dv}{J} \end{aligned} \quad . \quad (15)$$

Here, $\mathbf{c}$ is the 4th order spatial elasticity tensor [1]:

$$\mathsf{c}_{ijkl} = \frac{4}{J}F_{iI}F_{jJ}F_{kK}F_{lL}\frac{\partial^2 W}{\partial C_{IJ}\partial C_{KL}}\,, \quad (16)$$

and $\nabla^s[\cdot]$ is the symmetric gradient operator:

$$\nabla^s[\cdot] = \frac{1}{2}\left[\frac{\partial[\cdot]}{\partial \boldsymbol{\varphi}} + \left(\frac{\partial[\cdot]}{\partial \boldsymbol{\varphi}}\right)^T \right]. \quad (17)$$

In the field of computational mechanics, the first two terms in the second line of equation (15) are referred to as the *geometric* and *material stiffnesses*, respectively

[1]. The 2nd order tensor representing the image stiffness for hyperelastic Warping is:

$$\mathbf{k} = \frac{\partial^2 U}{\partial\boldsymbol{\varphi}\partial\boldsymbol{\varphi}} = \lambda\left[\left(\frac{\partial S}{\partial\boldsymbol{\varphi}}\right)\otimes\left(\frac{\partial S}{\partial\boldsymbol{\varphi}}\right)-\left(T-S\right)\left(\frac{\partial^2 S}{\partial\boldsymbol{\varphi}\partial\boldsymbol{\varphi}}\right)\right]. \tag{18}$$

These three terms form the basis for evaluating the relative influence of the image-derived forces and the forces due to internal stresses on the converged solution to the deformable image registration problem, as illustrated in the following two sections.

2.5. Finite Element Discretization

Hyperelastic Warping is based on an FE discretization of the template image. The FE method uses "shape functions" to describe the element shape and the arbitrary variations in configuration over the element domain [34]. In hyperelastic Warping, an FE mesh is constructed to correspond to all or part of the template image (either a rectilinear mesh, or a mesh that conforms to a particular structure of interest in the template image). The template intensity field T is interpolated to the nodes of the FE mesh. The template intensity field is convected with the FE mesh and thus the nodal values do not change. As the FE mesh deforms, the values of the target intensity field S are queried at the current location of the nodes of the template FE mesh. To apply an FE discretization to equation (15), an isoparametric conforming FE approximation is introduced for the variations $\boldsymbol{\eta}$ and $\Delta\boldsymbol{u}$:

$$\boldsymbol{\eta}_e \equiv \boldsymbol{\eta}\,|_{\Omega_e} = \sum_{j=1}^{N_{\text{nodes}}} N_j\left(\xi\right)\boldsymbol{\eta}_j, \qquad \Delta\boldsymbol{u}_e \equiv \Delta\boldsymbol{u}\,|_{\Omega_e} = \sum_{j=1}^{N_{\text{nodes}}} N_j\left(\xi\right)\Delta\boldsymbol{u}_j\,, \tag{19}$$

where the subscript e specifies that the variations are restricted to a particular element with domain Ω_e, and N_{nodes} is the number of nodes composing each element.

Here, $\boldsymbol{\xi} \in \square$, where $\square := \{(-1,1)\times(-1,1)\times(-1,1)\}$ is the bi-unit cube and N_j are the isoparametric shape functions (having a value of "1" at their specific node and varying to "0" at every other node). The gradients of the variation $\boldsymbol{\eta}$ are discretized as

$$\nabla_s \boldsymbol{\eta} = \sum_{j=1}^{N_{\text{nodes}}} \boldsymbol{B}_j^L \boldsymbol{\eta}_j, \qquad \nabla \boldsymbol{\eta} = \sum_{j=1}^{N_{\text{nodes}}} \boldsymbol{B}_j^{NL} \boldsymbol{\eta}_j . \tag{20}$$

Where $\boldsymbol{B}^L$ and $\boldsymbol{B}^{NL}$ are the linear and nonlinear strain-displacement matrices, respectively, in Voigt notation [1] (see Appendix). With the use of appropriate Voigt notation, the linearized equations (15) can be written, for an assembled FE mesh, as:

$$\sum_{i=1}^{N_{\text{nodes}}} \sum_{j=1}^{N_{\text{nodes}}} \left(\boldsymbol{K}^R \left(\boldsymbol{\varphi}^*\right) + \boldsymbol{K}^I \left(\boldsymbol{\varphi}^*\right) \right)_{ij} \cdot \Delta \boldsymbol{u}_j = \sum_{i=1}^{N_{\text{nodes}}} \left(\boldsymbol{F}^{\text{ext}} \left(\boldsymbol{\varphi}^*\right) + \boldsymbol{F}^{\text{int}} \left(\boldsymbol{\varphi}^*\right) \right)_i \tag{21}$$

Equation (21) is a system of linear algebraic equations. The term in parentheses on the left-hand side is the (symmetric) tangent stiffness matrix. $\Delta \boldsymbol{u}$ is the vector of unknown incremental nodal displacements – for an FE mesh of 8-noded hexahedral elements in three dimensions, $\Delta \boldsymbol{u}$ has length [8x3xN_{el}], where N_{el} is the number of elements in the mesh. $\boldsymbol{F}^{\text{ext}}$ is the vector of external forces arising from the differences in the image intensities and gradients in equation (12), and $\boldsymbol{F}^{\text{int}}$ is the vector of internal forces resulting from the stress divergence. The material and geometric stiffnesses combine to give the mechanics regularization stiffness:

$$\boldsymbol{K}^R = \int_{\boldsymbol{\beta}} \left(\boldsymbol{B}^{NL}\right)^T \boldsymbol{\sigma} \boldsymbol{B}^{NL} dv + \int_{\boldsymbol{\beta}} \left(\boldsymbol{B}^{L}\right)^T \mathbf{c} \boldsymbol{B}^{L} dv . \tag{22}$$

The contribution of the image-based energy to the tangent stiffness is:

$$\boldsymbol{K}^{I} = -\int_{\beta} \boldsymbol{N}^{T} \mathbf{k} \boldsymbol{N} \frac{dv}{\mathrm{J}}. \tag{23}$$

Together, the terms in (22) and (23) form the entire tangent stiffness matrix. In our FE implementation, an initial estimate of the unknown incremental nodal displacements is obtained by solving equation (21) for $\Delta \boldsymbol{u}$ and this solution is improved iteratively using a quasi-Newton method [27].

2.6. Solution Procedure and Augmented Lagrangian

In the combined energy function in Equation (9), the image data may be treated as either a soft constraint, with the mechanics providing the "truth", as a hard constraint, with the mechanics providing a regularization, or as a combination. For typical problems in deformable image registration, it is desired to treat the image data as a hard constraint. Indeed, the form for U specified in equation (8) is essentially a penalty function stating that the template and target image intensity fields must be equal over the domain of interest as $\lambda \to \infty$. The main problem with the penalty method is that as the penalty parameter λ is increased, some of the diagonal terms in the stiffness matrix $\boldsymbol{K}_I$ become very large with respect to others, leading to numerical ill-conditioning of the matrix. This results in inaccurate estimates for $\boldsymbol{K}_I^{-1}$, which leads to slowed convergence or divergence of the nonlinear iterations.

To circumvent this problem, the augmented Lagrangian method is used [33, 35]. With augmented Lagrangian methods, a solution to the governing equations at a particular computational timestep is first obtained with a relatively small penalty parameter λ. Then the total image-based body forces $\partial U/\partial \boldsymbol{\varphi}$ are incrementally increased in a second iterative loop, resulting in progressively better satisfaction of the constraint imposed by the image data. This leads to a stable algorithm that allows the constraint to be satisfied to a user-defined tolerance. Ill conditioning of the stiffness matrix is entirely avoided.

The Euler-Lagrange equations defined in Equation (13) are modified by the addition of a term that represents the additional image-based force γ due to the augmentation:

$$G^{*} = G(\boldsymbol{\varphi},\boldsymbol{\eta}) + \int_{\beta} \gamma \cdot \boldsymbol{\eta} \frac{dv}{J} = 0 \tag{24}$$

The solution procedure involves incrementally increasing γ at each computational timestep and then iterating using a quasi-Newton method [27] until the energy is minimized. In the context of the FE method described above, the augmented Lagrangian update procedure for timestep n+1 takes the form:

$$\boxed{\begin{array}{l} \gamma_{n+1}^{0} = \gamma_{n} \\ k = 0 \\ \text{DO for each augmentation } k \text{ WHILE } \left\| \left(\gamma_{n+1}^{k+1} - \gamma_{n+1}^{k}\right) / \gamma_{n+1}^{k} \right\| > \text{TOL} \\ \quad \text{Minimize } G^{*} \text{ with } \gamma_{n+1}^{k} \text{ fixed using the BFGS method} \\ \quad \text{Update mutipliers using } \gamma_{n+1}^{k+1} = \gamma_{n+1}^{k} + \left(\partial U/\partial \boldsymbol{\varphi}\right)_{n+1}^{k} \\ \text{END DO} \end{array}} \tag{25}$$

This nested iteration procedure, referred to as the Uzawa algorithm [36, 37], converges quickly in general because the multipliers γ are fixed during the minimization of G^{*}. In practice, the augmentations are not performed until the penalty parameter λ has been incremented to the maximum value that can be obtained without solution difficulties due to ill conditioning. At this last timestep, the augmented Lagrangian method is then used to satisfy the constraint to a user-defined tolerance (usually TOL = 0.05).

2.7. Sequential Spatial Filtering to Overcome Local Minima

The solution approach described above follows the local gradient to search for a minimum in the total energy (Equation (4)) and therefore it is susceptible to converging to local minima. This means that the registration process may get “stuck” by alignment of local image features that produce forces locking the deformation into a particular configuration. It is often possible to avoid local minima and converge to a global minimum by first registering larger image features, such as object boundaries and coarse textural detail, followed by registration of fine detail. Sequential low-pass spatial filtering is used to achieve this goal. By evolving the cut-off frequency of the spatial filter over computational time, the influence of fine textural features in the image can be initially suppressed until global registration is achieved. Fine structure can be registered subsequently by gradually removing the spatial filter.

The spatial filter is applied by convolution of the image with a kernel $\kappa(\boldsymbol{X})$. For the template image field T,

$$T^*(\mathbf{X}) = T(\mathbf{X}) * \kappa(\mathbf{X}) = \int_B T(\mathbf{X})\kappa(\mathbf{X}-\mathbf{Z})d\mathbf{Z} \ , \tag{26}$$

where $T(\boldsymbol{X})$ and $T^*(\boldsymbol{X})$ are the original image data and the filtered data respectively in the spatial domain; $\boldsymbol{X}$ is a vector containing the material coordinates and $\boldsymbol{Z}$ is the frequency representation of $\boldsymbol{X}$. An efficient way to accomplish this calculation is through the use of the discrete Fourier transform.

The convolution of the image data $T(\mathbf{X})$ with the filter kernel $\kappa(\mathbf{X})$ in equation (26) becomes multiplication of $T(\mathbf{Z})$ with $\mathrm{K}(\mathbf{Z})$ in Fourier domain. $T(\mathbf{Z})$ is the Fourier transform of $T(\mathbf{X})$ and $\mathrm{K}(\mathbf{Z})$ is the Fourier transform of $\kappa(\mathbf{X})$. This multiplication is applied and then the transform is inverted to obtain the convolved image in the spatial domain as shown below:

$$T^*(\mathbf{X}) = \Im^{-1}\{T(\mathbf{Z})\mathrm{K}(\mathbf{Z})\}. \tag{27}$$

Because of the very fast computational algorithms available for applying Fourier transforms, this method is much faster than computing the convolution in image space. In our implementation, a 3D Gaussian kernel is used [38]:

$$\kappa\left(\boldsymbol{X}\right) = Ae^{\left(-\frac{\boldsymbol{X}\cdot\boldsymbol{X}}{2\sigma^2}\right)}. \tag{28}$$

Here, σ^2, the spatial variance, is used to control the extent of blurring while A is a normalizing constant. Note that Equation (28) is only valid for a 3D vector $\boldsymbol{X}$. The user specifies the evolution of the spatial filter over computational time by controlling the mask and variance. In the specific results reported below the variance was set to a high value and evolved to remove the filtering as the computation completed (Figure 2).

The practical application of spatial filtering is complicated by the fact that the registration is nonlinear and is computed stepwise during the registration process. At each step in the computational process, the spatial distribution of the template intensities changes according to the computed deformation field. Therefore, all image operations done on the template during the registration process (including spatial filtering techniques) must be performed on the deformed template image, rather than the static template image before deformation. Since, in most cases, the template finite element mesh nodes are not co-located with the template image voxels, the computed deformation field must be interpolated onto the original

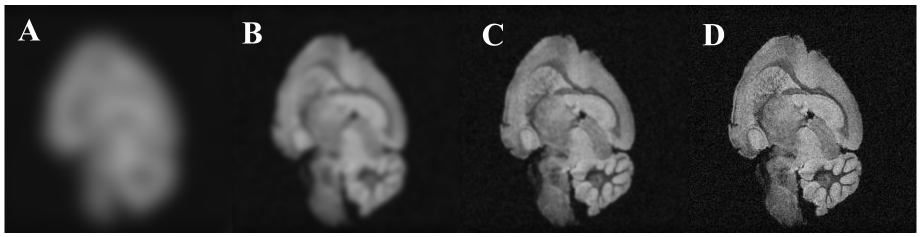

Figure 2: Sequential spatial filtering. (A) results of a 10 x 10 pixel mask flat blur to suppress the local detail in the original image (D). (B) 5 x 5 mask, (C) 2 x 2 pixel mask, and (D) original image.

template image in order to apply the image operations accurately.

2.8. Regular versus Irregular Meshes

Hyperelastic Warping accommodates an FE mesh that corresponds to all or part of the template image. A "regular mesh" is a rectilinear structured mesh that corresponds to the entire image domain. This mesh may be a subsampling of the actual image voxel boundaries. An "irregular" mesh conforms to a particular structure of interest in the template image. The template intensity field T is interpolated to the nodes of the FE mesh. As the FE mesh deforms, the values of the target

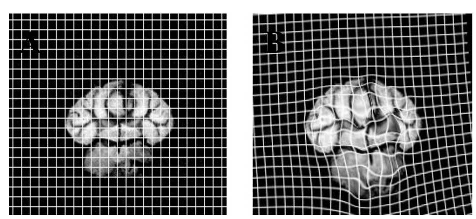

Figure 3: (A) Template and (B) deformed images of a normal mouse brain cross-section with a representation of a regular finite element mesh superimposed upon the image.

intensity field S are sampled at the current location of the nodes of the template FE mesh.

Regular meshes are used primarily for non-physical deformable image problems (Figure 3). Regular meshes are simple to construct and can easily span the entire image space or a specific region of interest. However, since the mesh does not conform to any structure in the template imaged, these analyses are susceptible to element inversion prior to the completion of image registration. Typically, only a single material is generally used for the entire mesh.

In contrast to regular meshes, irregular meshes are used primarily for physical deformation applications and conform to physical structures of interest in the domain of the image data (Figure 4). Irregular meshes also support the definition of different material models and material properties for specific regions of the mesh. For example, in Figure 4, the irregular mesh represents a cross-section of a human coronary artery. It has two materials, each representing separate layers of the arterial wall. Each layer was assigned material properties from the literature that are appropriate for that specific layer [39]. The primary drawback of irregular meshes is that, depending upon the

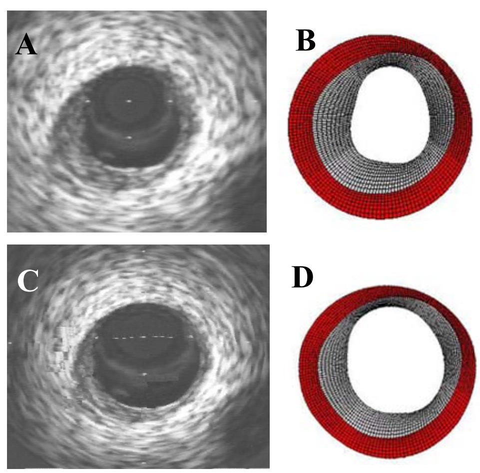

Figure 4: A - Intravascular ultrasound cross-sectional image of coronary artery. B - Finite element model of Template image. C - Deformed image of artery after application of 100 mmHg internal pressure load. D - Deformed finite element model after hyperelastic warping analysis. The grey area of the arterial wall is represents the intima while the red region represents the adventitia.

geometry to be modeled, they can be time consuming to construct.

2.9. Rezoning Regular Finite Element Meshes

The large deformations that occur in the context of many deformable image registration problems can result in "element inversion" prior to complete registration. Element inversion is the generation, via deformation during the solution process, of a finite element that has a negative Jacobian. Physically, for hexahedral elements this implies an angle of greater than 180° between two adjacent edges of an element. This condition halts the solution process and thus must be remedied in order to proceed.

To overcome this problem when regular meshes are used, an FE rezoning algorithm has been implemented. The algorithm allows the tracking of large-scale deformations using a relatively coarse computational mesh. When element inversion is imminent, the FE mesh geometry is reset to its initial undeformed configuration and the deformed template image intensity T and nodal displacements $\boldsymbol{u}(\boldsymbol{X})$ are interpolated from the deformed mesh to the reset mesh. The analysis then continues until the convergence criteria are met or another rezoning is required. The rezoning

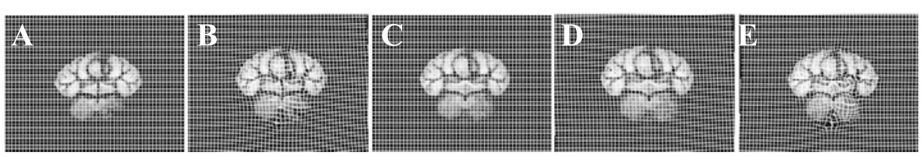

Figure 5: Example of rezoning a regular mesh for a 2D Warping problem. (A) Template image with a representation of the FE mesh superimposed on the image. (B) The registration process causes large deformations in the computational mesh. (C) The mesh is reset and the analysis continues. (D) Rezoning allows for greater overall deformation during the registration process. (E) Deformed template image at the end of the analysis.

process is illustrated graphically in Figure 5.

The rezoning procedures require interpolation of T and $\boldsymbol{u}(\boldsymbol{X})$ from the nodes of the deformed FE mesh to the nodes of the reset mesh. For each node N in the undeformed mesh, the element in deformed mesh that contained the node is located using a direct search. The local coordinates of the eight nodes of the element containing node N are assembled into an 8x3 matrix $\boldsymbol{\phi}(\xi_i, \eta_i, \zeta_i)$, where ξ_i, η_i, and ζ_i are the local element coordinates of the nodes composing the element; for instance, node 1 has local coordinates (-1,1,1). The local coordinates are related to the global coordinates via the interpolating polynomial coefficients arising from the shape functions as follows [40]:

$$[\boldsymbol{\phi}] = [\boldsymbol{G}][\boldsymbol{\alpha}] \Leftrightarrow$$
$$\begin{bmatrix} -1 & 1 & 1 \\ . & . & . \\ . & . & . \\ 1 & 1 & 1 \end{bmatrix} = \begin{bmatrix} 1 & x_1 & y_1 & z_1 & xy_1 & yz_1 & xz_1 & xyz_1 \\ . & . & . & . & . & . & . & . \\ . & . & . & . & . & . & . & . \\ 1 & x_8 & y_8 & z_8 & xy_8 & yz_8 & xz_8 & xyx_8 \end{bmatrix} \begin{bmatrix} \alpha_1 & \beta_1 & \gamma \\ . & . & . \\ . & . & . \\ \alpha_8 & \beta_8 & \gamma_8 \end{bmatrix} \quad (29)$$

Here, $\boldsymbol{\alpha}$ is an 8x3 matrix containing the polynomial coefficients and (x_i, y_i, z_i) are the coordinates of node i in the global coordinate system. The matrix $\boldsymbol{\alpha}$ is then determined for each node N in the reset mesh:

$$[\alpha] = [G]^{-1}[\phi]. \quad (30)$$

The local element coordinates (ξ_N, η_N, ζ_N) of node N follow from $\boldsymbol{\alpha}$ and the global coordinates (x_N, y_N, z_N):

$$
\begin{bmatrix}\zeta_N & \eta_N & \xi_N\end{bmatrix} = \begin{bmatrix}1 & x_N & y_N & z_N & xy_N & yz_N & xz_N & xyz_N\end{bmatrix}\begin{bmatrix}\alpha_1 & \beta_1 & \gamma \\ \alpha_2 & \beta_2 & \gamma_2 \\ . & . & . \\ . & . & . \\ . & . & . \\ \alpha_8 & \beta_8 & \gamma_8\end{bmatrix}. \tag{31}
$$

The interpolated value then follows from the local coordinates, the nodal values and the trilinear shape functions. For example, the interpolated template intensity is computed using

$$
T_N\left(\xi_{\mathrm{N}}, \eta_{\mathrm{N}}, \zeta_{\mathrm{N}}\right) \ = \sum_{i=1}^{8} T_i \, h_i\left(\xi_{\mathrm{N}}, \eta_{\mathrm{N}}, \zeta_{\mathrm{N}}\right), \tag{32}
$$

where the T_{i} are nodal intensity values and h_{i} are the shape functions corresponding to each node evaluated at $\left(\xi_{\mathrm{N}}, \eta_{\mathrm{N}}, \zeta_{\mathrm{N}}\right)$. The displacements $\boldsymbol{u}(\boldsymbol{X})$ are interpolated using the same procedure. Note that this interpolation strategy is consistent with the shape functions used in the FE solution process.

In practice, this rezoning procedure has proved to be highly efficient and effective for large three-dimensional Warping problems. It has allowed for the registration of image data sets that otherwise could not be successfully registered using hyperelastic Warping. In the first example found below, rezoning allowed for the successful inter-subject registration of mouse brain micro-MRI images. Analysis of these image data sets without rezoning led to incomplete registration of the internal structure of the brain as well as incomplete external registration of the cerebellum.

3. Applications

The following examples illustrate the broad range of problems that have been analyzed using hyperelastic Warping. The first example is an image registration problem in which MRI images of two normal mouse brains were registered. The second example illustrates how the results of a registration analysis of micro-CT images of the gerbil middle ear may be used to provide the boundary conditions for a second, traditional FE analysis of the malleus bone. The remaining examples illustrate application to problems in cardiovascular mechanics.

3.1. Quantification of Changes in Mouse Brain Morphology

Quantification of time-dependent changes in three-dimensional morphology of brain structures and neural pathways is a fundamental challenge in anatomical studies of neurodevelopment and in tracking brain remodeling and/or progression of certain neurological diseases. The morphometric problem can be approached using *in vivo* gross-scale (sub-millimeter) magnetic resonance medical imaging (MRI) of the brain. Tracking anatomical changes *in vivo* has been a major motivation for the development of higher resolution CT, MRI and radiographic imaging systems. While it is currently routine in clinical MRI of humans to obtain 1x1x2 mm resolution, micro-MRI images of small animals have been obtained with isotropic resolution on the order of 40 microns – resolution sometimes termed *magnetic resonance microscopy* (MRM). This type of MRI data is sufficient to resolve the neuroanatomical structures of interest but it remains difficult to extract quantitative structure-specific morphological measures directly from this type of image data. These measures are necessary to accurately assess developmental and/or pathological changes in gross brain structures and pathways.

In order to test the efficacy of hyperelastic Warping in the registration of normal mouse brain anatomy, normal T_1-weighted micro-MRI images were obtained from two different intact, excised mouse brains. The image datasets were 256^3 voxels, FOV=1.54x1.54x1.54 cm, and had 60 μm isotropic resolution. A 40x40x49 rectilinear FE mesh was created for the 3D problems (73,008 elements). The deforming template was modeled using a neo-Hookean hyperelastic material with a shear modulus of 450 Pa and a bulk modulus of 400 Pa [22].

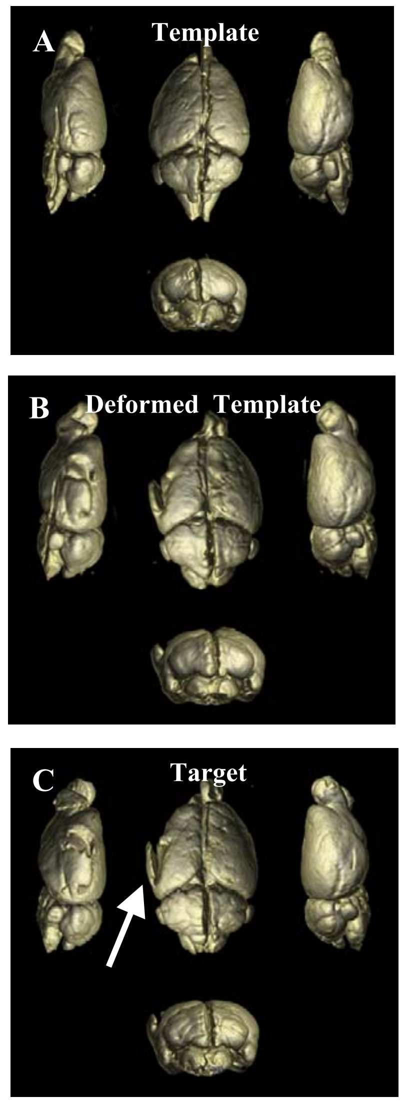

Figure 6. Three dimensional results for inter-animal registration of two mouse neuroanatomies. (A) Surface-rendered template, (B) deformed template, and (C) target image. The arrow indicates the

These 3D results demonstrate the efficacy of the current deformable image registration algorithm when used on relatively large datasets. Volume-rendered images (Figures 6) show that excellent external registration was achieved between the deformed template and target image datasets. The 3D model was rezoned three times to achieve this registration. It is interesting to note that rezoning allowed a dissection artifact in the target image dataset (Figure 6C), that was not present in the template image data (Figure 6A), to be extruded from the relatively smooth template to generate the same structure in the deformed template (Figure 6B). Without the use of rezoning, this excellent alignment would have been impossible due to extreme mesh distortion resulting in element inversion. Examination of representative transverse and longitudinal image planes illustrated that very good internal registration was also achieved, as demonstrated by the correspondence of anatomical regions and sulci between the deformed template and target (Figure 7, panels A-D).

Computational requirements for this problem were determined primarily by the size of the finite element mesh used to discretize the template and, to a lesser extent, by the size of the image datasets. The analysis required 3.38 GB of memory. Because the main computational expense in the algorithm is the inversion of a large system of linear equations resulting

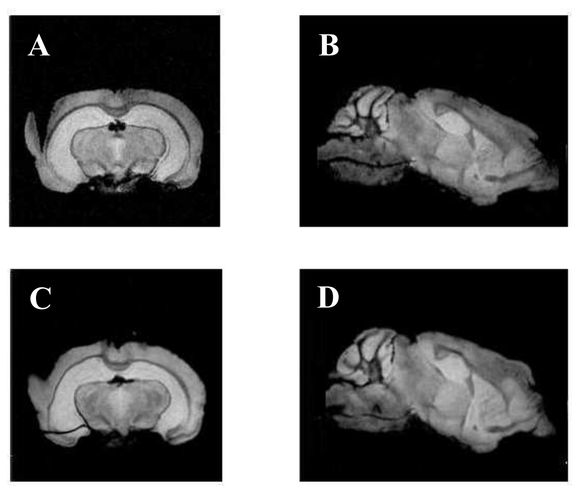

Figure 7. A mid-brain cross-section from a normal mouse (A) and a longitudinal section (B) from the 3-D target image data and the corresponding deformed template (C and D).

from the nodal degrees of freedom in the FE mesh, CPU requirements grew as the square of the size of the FE mesh. For this analysis, the mesh resulted in a linear system with 165,148 degrees of freedom. Total wall clock time for the 3D neuroanatomical registration analysis was 14 hours, with the three mesh rezones accounting for 18% of the analysis time and the sequential spatial filtering accounting for 5% of the analysis time. The vast majority of the remaining analysis time is spent in the repeated inversion of the sparse symmetric linear system. Our code accommodates the use of several vendor supplied parallel solvers, which can reduce the time for this phase of the solution process drastically. The analysis time can be further reduced by the reduction of the size of the computational mesh, at the potential expense of reducing the accuracy of the registration of internal structures.

3.2. Measurement of Gerbil Malleus Kinematics and Mechanics

The human auditory system is capable of transforming and distinguishing incoming acoustical signals over several orders of magnitude. The middle ear, in particular, acts as an impedance matching transformer, allowing the mechanical vibrations of the tympanic membrane to be transformed into liquid-borne traveling waves within the cochlea. These traveling waves are in turn transformed into neural signals that the brain interprets as sound.

Finite element models have been used to study the kinematics of the middle ear bones in order to gain a better understanding of the impedance matching function of the middle ear [41-44]. These models consist of 2D and 3D finite element representations of the individual bones and muscles of the middle ear as well as the tympanic membrane. The natural frequencies of the eardrum have been measured and used to excite finite element representations of the tympanic membrane to study the frequency response and kinematics of the middle ear bones [41, 42]. Ladak and Funnell [45] modeled the normal and surgically repaired cat middle ear in order to study the effects of ossicular prosthetics on the frequency response of the ossicular chain. While direct measurements of the geometry and kinematics of the tympanic membrane has been demonstrated, measurements of the kinematics of the middle ear bones themselves have proven to be more difficult. Toward this end, the following study was designed to examine the feasibility of using hyperelastic Warping to determine the displacements of the ossicular chain using warping analysis of high-resolution CT images. These displacements would in turn provide the boundary conditions for FE models of the individual bones of the ossicular chain. This secondary analysis would be used to determine the stress distributions within bones of the middle ear. High-resolution computed tomography (CT) images (1024 x 1024 x 1024 isotropic image matrix, 14.1 mm FOV, 10 μm isotropic resolution) were taken of the external and middle ear of an anesthetized gerbil. The images were acquired on a Skyscan 1072 80 kV micro-CT tomograph. An image data set was acquired with the tympanic membrane under no external pressure load other than atmospheric pressure. The second image set was acquired while a 3.0 KPa pressure load was placed on the external surface of the tympanic membrane. The images were cropped (270x270x172 voxels) to include only the tympanic membrane and the malleus bone of the middle ear. The image obtained under atmospheric

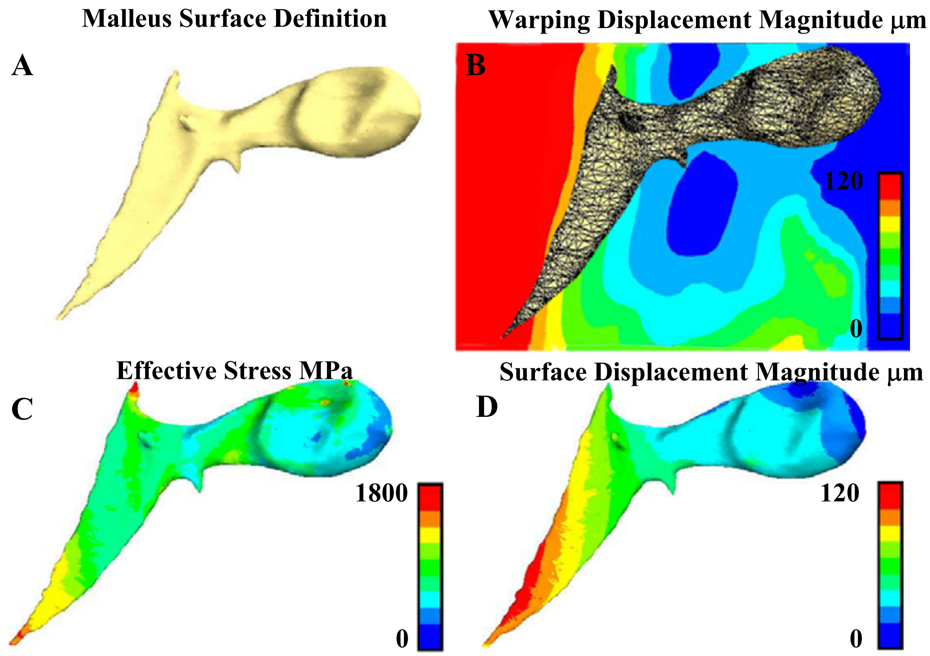

Figure 8. (A) Rendered surface definition of the gerbil malleus. (B) Displacement magnitude warping results for a plane bisecting the center of the malleus. The tetrahedral mesh has been superimposed on the results to indicate the location of the malleus within the displacement field. (C) Effective stress and (D) displacement magnitude results for the surface of the malleus.

loading was defined as the template image while the image under a pressure load of 3 KPa was defined as the target image. A 41x41x27 rectilinear finite element mesh was constructed that included the entire cropped image domain (11767 elements). This deforming template mesh was modeled as a neo-Hookean hyperelastic material with a shear modulus of 450 Pa and a bulk modulus of 400 Pa. A fixed flat spatial filter (3x3x3 pixel mask) [38] was used in the warping analysis. The FE mesh was rezoned twice during the analysis to determine the displacements of the malleus.

Subsequent to the deformable registration analysis, a finite element model was created to represent the malleus bone. The external boundary of the malleus was manually segmented from the *template* image data set. B-spline curves were fit to the points generated by the segmentation and these curves were used to define the exterior surface of the malleus. A tetrahedral mesh (42,391 elements) was generated from this surface definition. The malleus was modeled as a linear elastic material using properties (elastic modulus E = 20.0 GPa, Poisson's Ratio, ν = 0.3) from the literature [41, 45].

The surface of the malleus model was loaded using the displacements determined from the deformable image registration analysis. The displacements for each surface node of the malleus model were defined by interpolating nodal displacements determined from the warping analysis using the rectilinear (Warping) mesh trilinear shape functions. The NIKE3D non-linear finite element program [46] was used to analyze the malleus model and determine the stress/strain distribution within the bone using only the surface displacements as the boundary conditions.

The results indicate that the manubrium, which is at the center of tympanic membrane, undergoes the greatest displacement and is a high stress region of the malleus (Figure 8C and 8D). In contrast, the head of the malleus, which has attachments to the head of the incus and the superior ligament, shows the least displacement and is a low stress region. These results suggest that the malleus acts to decrease the energy being transferred to the incus. Further, this analysis demonstrates how the deformation map from a deformable image registration analysis using hyperelastic Warping can be integrated into a traditional computational biomechanics analysis using the FE method.

3.3. Strain Measurement of the Coronary Artery using Intravascular Ultrasound

Coronary heart disease is currently the leading cause of death in the United States [47]. Plaque rupture, the structural failure of the plaque cap, is the primary event triggering myocardial infarctions and acute coronary syndromes. The failure of the cap exposes collagen and lipid to the blood stream, which subsequently causes thrombus formation [48], often resulting in partial or complete blockage of the vessel. The exact mechanisms responsible for plaque rupture are unknown.

Finite element analyses of idealized plaque geometries have suggested that, for eccentric plaques, maximum stress levels occur at the shoulder area of the cap where the fibrous cap meets the healthy intima [49, 50]. Finite element analyses using model geometries based on atherosclerotic lesions indicate that the areas of high stress in and near the plaque correlate with the locations of plaque rupture. 58% of *in vivo* plaque ruptures have been to found occur in the areas of maximum stress, while 83% of failures occurred in high stress areas [51]. FE studies have suggested decreased cap thickness causes an increase in the peak shoulder stress when fully developed lipid layers are present. Similarly, increasing the lipid layer size increases the shoulder stress. [52-54].

Reliable predictions of stress and strain in physiologically loaded plaques in vivo would provide insight into plaque mechanics. Direct measurement of stress during loading of a coronary artery is currently not possible *in vivo* or *ex vivo*. However, the measurement of strain within the plaque and the wall of the coronary artery can provide insight into the stress distribution.

Intravascular ultrasound (IVUS) yields detailed images of atherosclerotic plaques and the vessel wall. IVUS uses a catheter-mounted ultrasound transducer to acquire cross-sectional images of an artery with a spatial resolution of 80-100 μm radially and 150-200 μm circumferentially [55, 56]. Current IVUS catheters are as small as 0.9 mm and can interrogate most areas of the coronary tree, including coronary arteries in the range of 1.5-5.0 mm in diameter. IVUS provides a high resolution means to quantify lesion geometry [55, 56]. Our long-term goal is to use hyperelastic Warping to determine the strain distributions within coronary plaque both *ex vivo* and *in vitro* during physiological loading as well as the loading associated with interventional techniques such as angioplasty and stent placement. The strain distributions can be correlated with the plaques histology to determine which plaque cap components are associated with the largest strain during loading. Hyperelastic Warping has been validated for use with IVUS and the details may be found in our previous publication [39].

Hyperelastic Warping was used to estimate the strain distributions in two unfixed left anterior descending (LAD) human coronary arteries. These arteries were mounted in a position approximating the artery orientation *in situ*. The left main coronary artery was cannulated, and the side branches were ligated to reduce flow until a constant physiological perfusion pressure could be maintained. IVUS images were acquired using a clinical IVUS system, comprising an HP Sonos 100 ultrasound console and a 30 MHz, 3.5 F Boston Scientific monorail intracoronary ultrasound imaging catheter using parameters typical for clinical study. The IVUS catheter was inserted into the vessel as halfway down the LAD. The arterial internal pressure monitored using a Millar 4 F pressure transducer introduced through a distal cannula placed approximately adjacent to the IVUS catheter. The vessel was then perfused with 37^{o}C physiological saline until a 16.00 KPa (120 mm Hg) internal pressure load was achieved. The IVUS images acquired under 0 KPa were designated the *template* images (Figure 9A and 10A), while the images acquired with the artery under 16.00 KPa (120 mmHg) internal pressure load were designated the *target* images (Figure 9B and 10B).

The boundaries of the media /lesion were manually segmented in the IVUS template image of the diseased vessels. B-spline curves were fitted to the points generated by segmentation. These curves defined the boundaries of the arterial wall. A 2D plane strain FE model was constructed for each vessel that included the entire image domain Figure 9C and 10C). The lumen and the tissue surrounding the vessels represented by an isotropic hypoelastic constitutive model with relatively soft elastic material properties (E=1.0 KPa and ν=0.3) to provide tethering. The outer edges of the image domain were fully constrained to eliminate rigid body motion. Transversely isotropic hyperelastic strain energy was utilized to describe nonlinear behavior of the arterial wall [57-64] and atherosclerotic lesions [50, 54, 65, 66]. This strain energy definition describes a material that consists of fibers imbedded in an isotropic ground substance. The strain energy function was defined as:

$$W = F_1(\tilde{I}_1, \tilde{I}_2) + F_2(\tilde{\lambda}) + \frac{K}{2}[\ln(J)]^2 \tag{33}$$

F_1 represents the behavior of the ground substance while F_2 represents the behavior of the collagen fibers. The final term in the expression represents the bulk behavior of the material. K is the bulk modulus of the material, $\boldsymbol{F}$ is the deformation gradient tensor and J = det($\boldsymbol{F}$). $\tilde{I}_1$ and $\tilde{I}_2$ are the first and second deviatoric invariants of the right Cauchy deformation tensor [30]. The scalar $\tilde{\lambda}$ is the deviatoric stretch ratio along the local fiber direction, ***a***, which was oriented circumferentially for these analyses to correspond with the collagen and smooth muscle fiber orientations in the arterial wall and plaque cap.

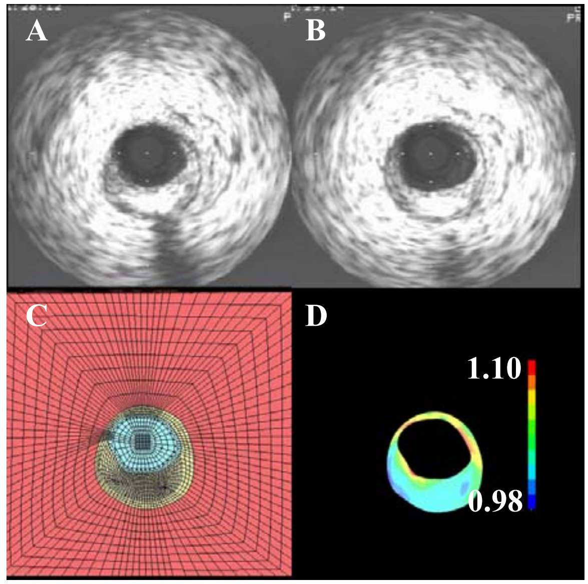

Figure 9. (A) template image of a coronary artery with a fully formed lipid layer (arrow). (B) Corresponding target image of the artery under 16.00 KPa internal pressure load. (C) FE mesh representation of the image space. (D) circumferential stretch distribution within the arterial wall and lesion.

A neo-Hookean form was used to represent the ground substance matrix:

$$F_1(\tilde{I}_1) = \mu(\tilde{I}_1 - 3). \tag{34}$$

Where μ is the shear modulus of the ground substance. The stress-stretch behavior for the fiber direction was represented as exponential, with no resistance to compressive load:

$$\begin{aligned} \tilde{\lambda} W_\lambda &= \tilde{\lambda} \frac{\partial F_2}{\partial \lambda} = 0, \quad \tilde{\lambda} < 1; \\ \tilde{\lambda} W_\lambda &= \lambda \frac{\partial F_2}{\partial \lambda} = C_3 \left[\exp\left(C_4 \left(\tilde{\lambda} - 1 \right) \right) - 1 \right], \ \tilde{\lambda} \geq 1. \end{aligned} \tag{35}$$

Where material coefficients C_3 and C_4 scale the fiber stress and control its rate of rise with increasing stretch, respectively. The full Cauchy stress tensor is defined as.

$$T = 2(W_1)B + \lambda W_\lambda a \otimes a + p1 \quad (36)$$

W_1, W_2 and W_λ are strain energy derivatives with respect to I_1, I_2 and λ [26], and $\boldsymbol{B}$ is the left deformation tensor. A detailed description of the finite element implementation of this constitutive model can be found in Weiss *et al.*[19].

The material parameters for the arterial wall were determined by a nonlinear least squares fit to circumferential stress/strain values presented in the work of Cox et al. [58] for the canine coronary artery wall using the constitutive relation described above. The media region of the arterial wall was assigned material properties based on the curve fit obtained from the Cox et al. data [57]. The material constants for the media were μ = 3.57 KPa, C_3 = 4.99 KPa, and C_4 = 5.49. The bulk modulus was defined as 200.00 KPa. The lesion areas were assigned identical material properties as were used for the media since the stress strain behavior of the arterial wall falls well within the wide range of values published for the material properties of atherosclerotic lesions [67].

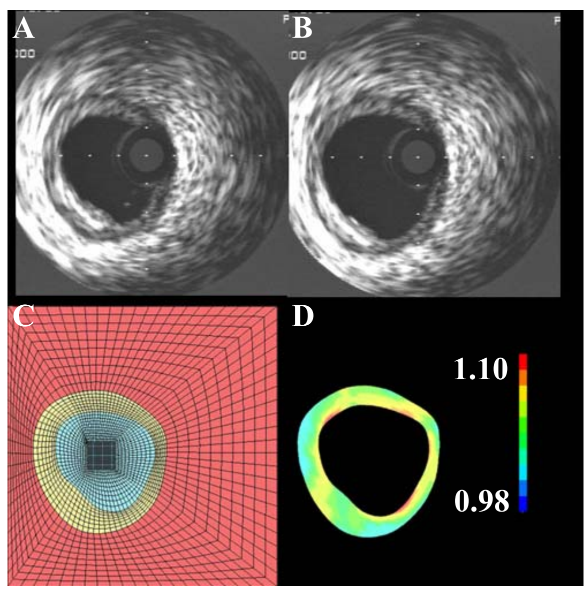

Figure 10. (A) Template image of a coronary artery that does not have a fully developed lipid core. (B) Corresponding target image of the artery under 16 KPa internal pressure load. (C) FE mesh of the image space. (D) Circumferential stretch distribution within the arterial wall and lesion.

The warping analyses results indicate (Figures 9D and 10D) that the presence of a fully developed lipid core increases the circumferential stretch of the plaque cap adjacent to the lipid core. These results are consistent with previous studies that suggested that the larger lipid layers increase plaque cap stress. [53, 54]

3.4. Cardiac Mechanics

Assessment of regional heart wall motion (wall motion, thickening, strain, etc.) can identify impairment of cardiac function due to hypertrophic or dilated cardiomyopathies. It can provide quantitative estimates of the impairment of ventricular wall function due to ischemic myocardial disease. The assessment regional heart motion is used in combination measures of perfusion and metabolic uptake to diagnose and evaluate stunned/hibernating myocardium following transient ischemic events. Stunned myocardium is characterized by decreased or no contractile function but having normal perfusion and glucose utilization [68-70]. Since stunned myocardium has normal perfusion and normal viability, it can only be identified by localizing abnormal wall motion/contraction. *Hibernating myocardium* is characterized by persistent ventricular myocardial dysfunction with preserved viability, decreased perfusion and normal metabolic uptake. Hibernating myocardium has been associated with a slower and incomplete restoration of contractile function as compared with stunned myocardium [71, 72]. Up to 50% of patients with ischemic heart disease and LV dysfunction have significant areas of hibernating myocardium [73, 74] and therefore would be predicted to benefit from identification and subsequent revascularization.

The assessment of the size and location of infarction, in particular, the extent of viable tissue, and the mechanical function of the tissue can be extremely valuable for predicting the utility and assessing the success of surgical interventions such as revascularization. Thus the measurement of local myocardial deformation has potential to be an important diagnostic and prognostic tool for the evaluation of a large number of patients.

The deformation of the human heart wall has been quantified via the attachment of physical markers in a select number of human subjects [75]. This approach provided valuable information but is far too invasive to be used in the clinical setting. With the development of magnetic resonance imaging (MRI) tagging techniques, non-invasive measurements of myocardial wall dynamics have been possible [76].

The most commonly clinically utilized techniques for the assessment myocardial regional wall motion and deformation of the myocardium are echocardiography and tagged MRI. LV wall function is typically assessed using 2-D Doppler echocardiography [77-82] through the interrogation of the LV from various views to obtain an estimate of the 3-D segmental wall motion. However, these measurements are not three dimensional in nature. Furthermore, echocardiography is limited to limited to certain acquisition windows

The most widely used approach for determining ventricular deformation is MR tagging [83-88]. MR tagging techniques rely on local perturbation of the magnetization of the myocardium with selective radio-frequency (RF) saturation to produce multiple, thin tag planes during diastole. The resulting magnetization reference grid persists for up to 400 ms and is convected with the myocardium as it deforms. The tags provide fiducial points from which strain can be calculated [85, 89]. The primary strength of tagging is that in vivo, noninvasive strain measurements are possible [85, 89]. The primary strength of MRI tagging is that noninvasive *in vivo* strain measurements are possible [85, 89]. It is effective for tracking fast, repeated motions in 3D. There are, however, limitations in the use of tagged MRI for cardiac imaging. The measured displacement at a given tag point contains only unidirectional information; in order to track the full 3D motion, these data have to be combined with information from other orthogonal tag sets over all time frames [76]. The technique's spatial resolution is coarser than the MRI acquisition matrix. Furthermore, the use of tags increases the acquisition time for the patient compared to standard cine-MRI, although improvements in acquisition speed have reduced the time necessary for image acquisition.

Sinusas *et al.* have developed a method to determine the strain distributions of the left ventricle using un-tagged MRI [90]. The system is a shaped based approach for quantifying regional myocardial deformations. The shape properties of the endo- and epicardial surfaces are used to derive 3-D trajectories, which are in turn used to deform a finite element mesh of the myocardium. The approach requires a segmentation of the myocardial surfaces in each 3-D image data set to derive the surface displacements.

Our long-term goal is to use hyperelastic Warping to determine the strain distribution in the normal left ventricle. These data will be compared with the left ventricular function due to the pathologies described above. Toward this end, the initial validation of the use of hyperelastic Warping with cardiac cine-MRI images is described.

3.4.1. Validation of Warping for Tracking Left Ventricular Deformation using Volumetric MRI

To validate the use of Warping for predicting LV strains from sets of volumetric cine-MRI images, a pair of 3D cine MRI image datasets representing two states of the left ventricle during the cardiac cycle was required. Further, the deformation map between the states represented in the images had to be known to provide a gold standard for comparisons. This was achieved by first acquiring a gated 3D cine-MRI dataset of a normal volunteer's heart during early diastole on a 1.5T Siemens scanner (256x256 image matrix, 378 mm FOV, 10 mm slice thickness, 10 slices). This volumetric MRI dataset was designated as the *template* image (Figure 11, left). The endocardial and epicardial surfaces of the LV were hand segmented. An FE model of the left ventricular (LV) image space was created based on these segmentations (Figure 12, left panel). The myocardium was represented as a transversely isotropic material with the fiber angle varying linearly from -90^o at the epicardial surface, through 0^o at the mid-wall, to 90^o at the endocardial surface [91]. The material coefficients were determined by least squares fit of the transversely isotropic hyperelastic constitutive model described in Weiss et al. [30] described above in the intravascular ultrasound section, to the

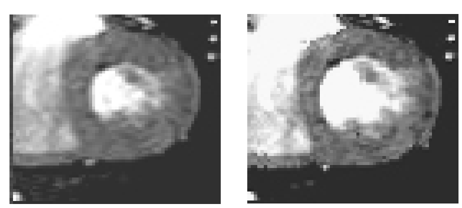

Figure 11. Mid-ventricular slices of the template (left) and the target (right) image datasets used in the validation analyses. Left image was obtained from direct MR volumetric image acquisition while right image was created by deforming left image using results of forward FE analysis (see text).

biaxial stress/strain values presented in the work of Humphrey et al. [31, 32].

An internal pressure load representing end-diastole was applied to the lumen and a standard "forward" nonlinear FE analysis was performed using the NIKE3D finite element program [92] (Figure 12). Using the deformation map obtained from the forward FE analysis, a deformed volumetric image dataset (target) was created by applying the deformation map to the original template MRI image (Figure 12, right panel).

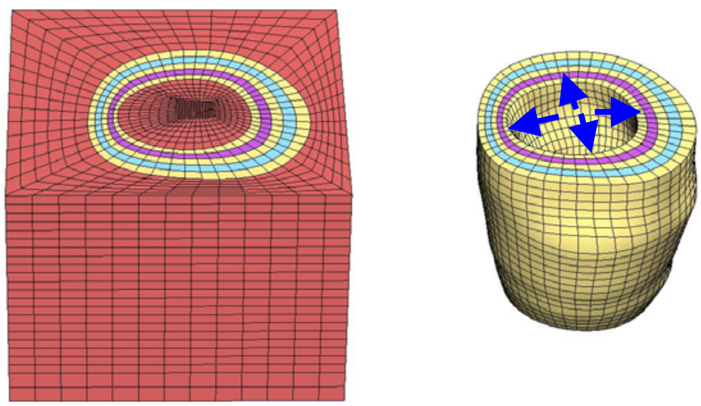

Figure 12: Left - FE mesh for forward model used to create target image. Right - A detailed view of the mesh corresponding to myocardial wall. Blue arrows indicate the pressure load applied to the endocardial surface.

A Warping model was created using the same geometry and material parameters that were used in the forward model described above. The Warping analysis was performed using the template image data set and a target image dataset was created by applying the forward model's deformation map to deform the template image. This yielded a template and target with a known solution for the deformations between them. The forward FE and Warping predictions of fiber stretch (final length/initial length along the local fiber direction) were compared to determine the accuracy of the technique. The validation results indicated good agreement between the forward and the warping fiber stretch distributions (Figure 13). A detailed analysis of the forward and predicted (Warping) stretch distributions for each image plane indicated good agreement (Figure 14).

To determine the sensitivity of the Warping analysis to changes in material parameters, μ and C_3 were increased and decreased by 24% of the baseline values. The 24% increase and decrease corresponds to the 95% confidence interval of material parameters determined from the least-squares fit of the material model to the Humphrey et al. data [31, 32]. Since, the proper material model is often not known for biological tissue, the material model was changed from the transversely isotropic model described above to an isotropic neo-Hookean material model. The analysis was repeated and the results compared with the forward model results.

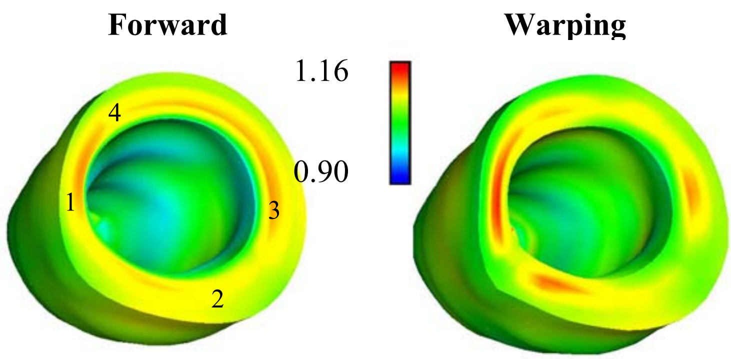

Figure 13: Fiber stretch distribution for the forward (left) and warping (right) analyses. The locations for the sensitivity analysis are shown on the forward model as numbers 1-4. Locations 5-8 are at the same locations as 1-4 but at the mid-ventricle level.

Location	1	2	3	4	5	6	7	8
	Upper Ventricle				Mid Ventricle			
Forward	1.09	1.06	1.12	1.07	1.08	1.04	1.02	1.05
μ+ 24%	1.09	1.09	1.13	1.07	1.07	1.03	1.03	1.05
μ- 24%	1.09	1.09	1.13	1.07	1.08	1.03	1.03	1.05
C_3 + 24%	1.09	1.08	1.13	1.08	1.08	1.03	1.03	1.05
C_3 - 24%	1.10	1.09	1.13	1.07	1.08	1.03	1.03	1.05
Neo-Hookean	1.10	1.07	1.13	1.07	1.07	1.02	1.02	1.05

Table 1: Effect of changes in material properties and material model on predicted fiber stretch. "Forward" indicates the forward FE solution, the "gold standard". Columns indicate locations 1-8 of the left ventricle, defined in the caption for Figure 3 above.

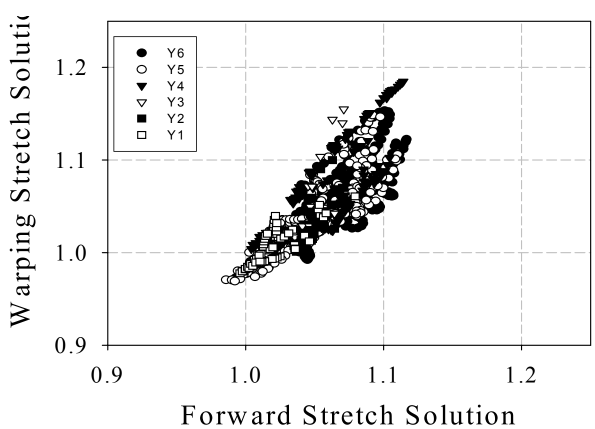

Figure 14. Comparison of Warping and forward nodal fiber stretch for each image slice. Y7 corresponds to the slice at the base of LV and Y1 is near the apex of the LV.

The forward and Warping sensitivity study results were compared at eight locations (Figure 13). These results show excellent agreement (Table 1) for all cases indicating hyperelastic Warping is relatively insensitive to changes to material model and material parameters. These results indicate that accurate predictions can be determined even when material model and parameters are not known. This is consistent with our previous results of Warping analyses of intravascular ultrasound images [22].

3.4.2. Myocardial Infarction

To study changes in systolic wall function due to myocardial infarction, a warping analysis was performed on a 3-D cine-MRI image data set for an individual with a lateral wall myocardial infarction (Male, 155 lbs, 51 y/o at time of scan, diabetic w/ small infarction.) The sub-endocardial infarction can be seen as the hyperenhancement of the lateral wall shown in the ce-MRI image (Figure 15A).

Delayed contrast enhanced MRI (ce-MRI) has been shown to be able to identify regions of infraction in the myocardium as hyperenhanced [93-96]. Furthermore, studies have indicated that the transmural extent of the hyperenhancement of ce-MRI predicts recovery of function after revascularization [97, 98] and can predict improved contractility post-revascularization [94].

To acquire the ce-MRI image data sets, the patients were placed supine in a 1.5T clinical scanner (General Electric) and a phased-array receiver coil was placed on the chest for imaging. A commercially available gadolinium-based contrast agent was administered intravenously at a dose of 0.2 mmol/kg and gated images were acquired 10-15 minutes after injection with 10 second breath holds. The contrast-enhanced images were acquired with the use of a commercially available segmented inversion-recovery sequence from General Electric. The 3-D cine-MRI image data sets for this patient were acquired on a 1.5T GE scanner (256x256 image matrix, 378 mm FOV, 10 mm slice thickness, 10 slices). The volumetric MRI dataset corresponding to

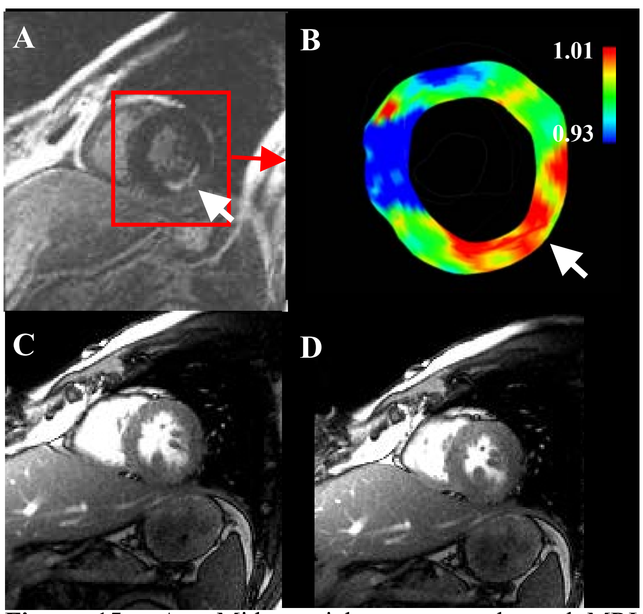

Figure 15: **A -** Mid-ventricle contrast-enhanced MRI image of the left ventricle. The hyperenhancement indicates the location of the infarction (arrow in left panel). **B -** Circumferential stretch distribution for systolic contraction filling. The arrow indicates the infarcted area of the lateral wall does not contract during systole. Mid-ventricle slices of the 3D cine MRI image data used for the systolic function analysis. **C** - Mid-systolic image (*template*). **D -** End-systolic image (*target*).

end-systole was designated as the *template* image (Figure 15C) while the image dataset corresponding to end-diastole was designated the *target* image (Figure 15D). A warping model and analysis was made using the methods detailed above.

The warping analysis reveals that the infarcted area undergoes little deformation during systole (circumferential stretch near 1.0). The analysis further reveals that the wall dysfunction extends over the lateral wall of the myocardium outside the area of hyperenhancement indicated in the ce-MRI images (Figure 15A). These results indicate that the contractile function of the heart is significantly impaired within and adjacent to the infarcted region.

4. Discussion and Conclusions

The finite element implementation hyperelastic Warping is a highly flexible registration method that can be used for the registration of physical and non-physical deformations. It makes use of either easily constructed regular meshes or irregular meshes that conform to the geometry of the structure being registered and can be used to register a particular region of interest or the entire of the image space. Additionally, hyperelasticity provides a physically realistic constraint for the registration of soft tissue deformation. Hyperelasticity based constitutive relations have been used to describe the behavior of a wide variety of soft tissues including the left ventricle [99-102], arterial tissue [103, 104], skin [105] and ligaments[106-109]. Hyperelastic Warping can be tailored to the type of soft tissue being registered through the appropriate choice of hyperelastic material model and material parameters.

Deformable image registration models based other material models have been used extensively in the field of anatomical brain registration. As was described above, an energy functional is minimized in order to achieve the registration solution. This functional consists of a measure of image similarity and an internal energy term (equation (4)). Measures of image similarity take the form of differences in the square of the image intensities (equation (8)) [15-17, 19, 110, 111] or are based on cross-correlation methods of the intensity or intensity gradient values [112]. Since the internal energy term of the energy functional is derived from the material model through the strain energy *W*, the registration process takes on the characteristics of the underlying material model. For example, registration methods that use a viscous or inviscid fluid constitutive model [15 , 17] have been shown to provide excellent registration results. However, these models have a tendency to underpenalize shear deformations and thus producing physically unrealistic registration of solids. In other words, the deformation of the deformable template resembles that of a fluid rather than that of a solid.

Other continuum based methods use linear elasticity [12, 13, 15, 16] to regularize registration. The use of linear elasticity is attractive due to the fact that it is relatively simple to implement. However, for the large deformations involved in inter- or intra-subject registration, it has a tendency to over-penalize large deformations. This is due to the fact that linear elasticity is not rotationally invariant. For an isotropic linear elastic material, the constitutive law is:

$$\boldsymbol{T} = \lambda tr(\boldsymbol{e}) + \mu \boldsymbol{e}. \tag{37}$$

Here, λ and μ are the Lamé material coefficients, and $\boldsymbol{e}$ is the infinitesimal strain "tensor" defined in terms of the displacement gradients. This infinitesimal strain is not a true tensor since it does not obey the transformation laws for 2nd order tensors. In detail:

$$\boldsymbol{e} = \frac{1}{2}\left(\left(\frac{\partial \boldsymbol{u}}{\partial \boldsymbol{X}}\right)^T + \frac{\partial \boldsymbol{u}}{\partial \boldsymbol{X}}\right). \tag{38}$$

But, $$\frac{\partial \boldsymbol{u}}{\partial \boldsymbol{X}} = \frac{\partial\left(\boldsymbol{x} - \boldsymbol{X}\right)}{\partial \boldsymbol{X}} = \boldsymbol{F} - \boldsymbol{1}. \tag{39}$$

For any deformation gradient $\boldsymbol{F}$, we can use the polar decomposition to write $\boldsymbol{F}$ as $\boldsymbol{F} = \boldsymbol{RU}$, where $\boldsymbol{R}$ is a proper orthogonal rotation and $\boldsymbol{U}$ is the positive definite symmetric right stretch tensor. With this substitution,

$$\boldsymbol{e} = \frac{1}{2}\left(\left(\boldsymbol{RU} - \boldsymbol{1}\right)^T + \left(\boldsymbol{RU} - \boldsymbol{1}\right)\right). \tag{40}$$

As indicated in equation (40), the strain $\boldsymbol{e}$ depends directly on $\boldsymbol{R}$, which describes the local rigid body rotation. As a result, even the smallest rotation of material axes induces stress in a linear elastic solid making the constitutive model non-objective.

This work has demonstrated that hyperelastic Warping may be used to analyze a wide variety of image registration problems using standard medical image modalities such as ultrasound, MRI and CT. The types of analyses demonstrated range from anatomical matching typical of non-physical image registration to the large physical deformations present in the deformation of the left ventricle over the cardiac cycle. As demonstrated in the presented work, the method allows for the estimation of the stress distribution within the structure(s) being registered, an attribute that has not demonstrated by other registration methods.

5. Acknowledgments

Financial support from NIH grant #R01-EB000121-14 (JAW, AIV) and NSF grant #BES-0134503 (JAW, AIV, NP) is gratefully acknowledged. An allocation of computer time was provided by the Center for High Performance Computing (CHPC) at the University of Utah. The authors would like to thank the following individuals for their contributions to this work and their continued collaboration: Grant T. Gullberg, Richard D. Rabbitt, Anton E. Bowden, Bradley N. Maker, Steve A. Maas, Geoffrey D. Vince, Robert J. Gillies, Edward V. R. DiBella, and Jean-Philippe Galons.

6. Question and Answer Section

Question 1: How are the principles of continuum mechanics used to regularize the deformable image registration problem involving the deformation of a template image into alignment with a target image? What are the primary advantages of this approach to regularization of the deformable image problem in comparison to ad-hoc methods?

Question 2: What is the purpose of the regularization term W in the deformable image registration problem?

Question 3: What is meant by treating the image data as a "hard constraint" in the deformable image registration problem?

Question 4: In hyperelastic Warping, in the limit as the penalty parameter $\lambda \to \infty$, the image-based energy converges to a finite value. Explain.

Question 5: Treating the image data as a hard constraint may cause the stiffness matrix to become ill-conditioned. How does the augmented Lagrangian method solve this problem?

Question 6: What is the role of the stiffness quantities in the solution procedure?

Question 7: How is sequential low pass filtering used in hyperelastic Warping to keep from converging to local minima in the solution?

Question 8: When using a regular mesh for hyperelastic Warping, why is rezoning needed?

Question 9: How is mechanical stress calculated with hyperelastic Warping?

Answers

Answer 1: A continuum mechanics-based approach models the template image as a deformable continuum that is analogous to a physical material. This method generates a one-to-one correspondence between template and target images and, with the use of appropriate constitutive models, is objective for arbitrarily large deformations and rotations.

Answer 2: Deformable image registration presents an ill-posed problem, which is solved by minimizing a potential energy cost function. Without regularization, this problem admits multiple solutions. W is the regularization term of the potential energy that constrains the solution space. This does not necessarily eliminate the possibility of multiple solutions, but it constrains the solution to provide solutions with some desirable quality (i.e., one-to-one mapping).

Answer 3: For hyperelastic Warping, the energy function $E = \int_{\boldsymbol{\beta}} W(\boldsymbol{X}, \boldsymbol{C}) \frac{dv}{J} - \int_{\boldsymbol{\beta}} U\left(T(\boldsymbol{X}), S(\boldsymbol{\varphi})\right) \frac{dv}{J}$ combines the effect of image data and the effect of mechanics. In order to reach a solution, a hard constraint of the image data is applied with the use of a penalty parameter in the image energy density functional. The mechanics is used to regularize the problem. By contrast, a solution could be reached for the image deformation problem by using the image data as a soft constraint and using mechanics to drive the solution.

Answer 4: The image energy density functional is given by $U(\boldsymbol{X},\boldsymbol{\varphi}) = \frac{\lambda}{2}\big(T(\boldsymbol{X}) - S(\boldsymbol{\varphi})\big)^2$. As the penalty parameter $\lambda \to \infty$, $\big(T(\boldsymbol{X}) - S(\boldsymbol{\varphi})\big)^2 \to 0$, and the image energy converges to a finite value.

Answer 5: As the penalty parameter λ is increased, some of the diagonal terms in the stiffness matrix $\boldsymbol{K}_I$ become very large with respect to others, leading to numerical ill-conditioning of the matrix. Augmented Lagrangian methods use a small penalty parameter λ to generate an initial solution at each computational timestep, then incrementally increase the image-based body force in an iterative loop.

Answer 6: The image stiffness is given $\mathbf{k} := \partial^2 U / \partial\boldsymbol{\varphi}\partial\boldsymbol{\varphi}$ and the regularization stiffness is $\mathbf{D} := \partial^2 W / \partial\boldsymbol{\varphi}\partial\boldsymbol{\varphi}$. These 2nd derivative terms (Hessians) describe how small perturbations of the current configuration affect the contributions of W and U to the overall energy of the system.

Answer 7: By using sequential low pass filtering, fine textural details are reduced and the image is first registered to larger image features. The cut-off frequency of the spatial frequency is then changed over computational time to remove the spatial filter and attain registration of fine textural detail after global registration is achieved.

Answer 8: Regular meshes are subject to element inversion during the solution process due to the fact that they often cross large intensity gradients in the image data and thus are subjected to large distortional forces during the registration process.

A rezoning algorithm resets the finite element mesh and interpolates the current results on the reset mesh, avoiding element inversion and thus allowing the image registration process to continue.

Answer 9: The template image is modeled as a deformable continuum with material properties defined via a hyperelastic strain energy function. Material properties combined with strain information from the finite element deformation yield stress distributions for the deformed image.

7. References

[1] Bathe, K. J., Finite Element Procedures, New Jersey, Prentice-Hall, 1996.

[2] Hadamard, J., Sur les problemes aux derivees partielles et leur signification physique, Bull. Univ. Princeton, Vol. 13, 1902.

[3] Hadamard, J., Le probleme de Cauchy et les equations aux derivees lineaires hyperboliques, Hermann, Paris, 1932.

[4] Grenander, U., Lectures in Pattern Theory I II and III: Pattern Analysis Pattern Synthesis and Regular Structures, Berlin Springer-Verlag, 1976.

[5] Grenander, U., Chow, Y. and Keenan, D., HANDS: A pattern theoretic study of biological shapes, New York, Springer-Verlag, 1990.

[6] Davatzikos, C., Spatial normalization of 3D brain images using deformable models, Journal of Computer Assisted Tomography, Vol. 20, No. 4, pp. 656-65, 1996.

[7] Davatzikos, C., Li, H. H., Herskovits, E. and Resnick, S. M., Accuracy and sensitivity of detection of activation foci in the brain via statistical parametric mapping: a study using a PET simulator, Neuroimage, Vol. 13, No. 1, pp. 176-84, 2001.

[8] Amit, Y., Graphical Shape Templates for Automatic Anatomy Detection with Applications to MRI Brain Scans, IEEE Transactions on Medical Imaging, Vol. 16, pp. 28-40, 1997.

[9] Tagare, H. D., Deformable 2-D template matching using orthogonal curves, IEEE Transactions on Medical Imaging, Vol. 16, pp. 108-117, 1997.

[10] Miller, M. I., Christensen, G. E., Amit, Y. and Grenander, U., Mathematical Textbook of Deformable Neuroanatomies Proceedings of the National Academy of Science Vol. 90, No. 24, pp. 144-48 1993.

[11] Hill, A., Cootes, T. F., Taylor, C. J. and Lindley, K., Medical image interpretation: a generic approach using deformable templates Medical Informatics Vol. 19, No. 1, pp. 47-59, 1994.

[12] Bajcsy, R., Lieberson, R. and Reivich, M., A computerized system for the elastic matching of deformed radiographic images to idealized atlas images, Journal of Computer Assisted Tomography, Vol. 7, No. 4, pp. 618-625, 1983.

[13] Bajcsy, R. and Kovacic, S., Multiresolution Elastic Matching, Computer Vision Graphics and Image Processing, Vol. 46, pp. 1-21, 1989.

[14] Gee, J. C. and Peralta, P. D., "Continuum models for Bayesian image matching," in *Maximum Entropy and Bayesian Methods*, K. M. Hanson and R. N. Silver, Dordrecht, Kluwer Academic Publishers, pp. 109-11, 1996.

[15] Christensen, G. E., Rabbitt, R. D. and Miller, M. I., 3D Brain Mapping Using a Deformable Neuroanatomy Physics in Medicine and Biology Vol. 39, pp. 609-618, 1994.

[16] Rabbitt, R. D., Weiss, J. A., Christensen, G. E. and Miller, M. I., Mapping of Hyperelastic Deformable Templates, Proceedings of SPIE International Society for Optical Engineering, Vol. 252, pp. 252-265, 1995.

[17] Christensen, G. E., Rabbitt, R. D. and Miller, M. I., Deformable Templates Using Large Deformation Kinematics, IEEE Transactions on Image Processing, Vol. 5, No. 10, pp. 1435-1447, 1996.

[18] Bowden, A. E., Rabbitt, R. D., Weiss, J. A. and Maker, B. N., Anatomical registration and segmentation by warping template finite element models, Proceedings of SPIE International Society for Optical Engineering, Vol. 3254, pp. 469-476, 1998.

[19] Weiss, J. A., Rabbitt, R. D. and Bowden, A. E., Incorporation of medical image data in finite element models to track strain in soft tissues, Proceedings of SPIE International Society for Optical Engineering Biomedical Optics Symposium BiOS98, Vol. 3254, pp. 477-484, 1998.

[20] Veress, A., Weiss, J., Gullberg, G., Vince, G. and Rabbitt, R., Validation for the Determination of Strain and Displacement Fields in Coronary Arteries Imaged by Intravascular Ultrasound, presented at American Society of Mechanical Engineering Biomedical Engineering Division Conference, Snowbird, UT, 2001.

[21] Veress, A. I., Weiss, J. A., Klein, G. J. and Gullberg, G. T., Quantification of 3D left ventricular deformation using hyperelastic warping:

Comparisons between MRI and PET imaging, presented at Computers in Cardiology, Memphis, TN, 2002.

[22] Veress, A. I., Weiss, J. A., Gillies, R. J., Bowden, A. E., Galons, J.-P. and Rabbitt, R. D., Quantification of Changes in Mouse Brain Morphology using MRI and Hyperelastic Warping, IEEE Transactions on Medical Imaging, In Press, 2004.

[23] Viegas, S. F., Hillman, G. F., Elder, K. and Stoner, D., Measurement of carpal bone geometry by computer analysis of three-dimensional CT images, Journal of Hand Surgery, Vol. 18, No. 2, pp. 341-349, 1993.

[24] Simo, J. C. and Hughes, T. J. R., Computational inelasticity, New York, Springer, 1998.

[25] Marsden, J. E. and Hughes, T. J. R., Mathematical Foundations of Elasticity, Minneola, NY, Dover, 1994.

[26] Spencer, A. J. M., Continuum mechanics, Essex England, Longman Scientific & Technical, 1980.

[27] Matthies, H. and Strang, G., The solution of nonlinear finite element equations, International Journal of Numerical Methods in Engineering, Vol. 14, pp. 1613-1626, 1979.

[28] Reddy, J. N., Energy and variational methods in applied mechanics, New York, Wiley, 1984.

[29] Lai, W. M., Introduction to Continuum Mechanics, New York, Permagon Press, 1993.

[30] Weiss, J., Maker, B. and Govindjee, S., Finite element implementation of incompressible transversely isotropic hyperelasticity, Computer Methods in Applications of Mechanics and Engineering, Vol. 135, pp. 107-128, 1996.

[31] Humphrey, J. D., Strumpf, R. K. and Yin, F. C., Determination of a constitutive relation for passive myocardium: II. Parameter estimation, Journal of Biomechanical Engineering, Vol. 112, pp. 340-6, 1990.

[32] Humphrey, J. D., Strumpf, R. K. and Yin, F. C., Determination of a constitutive relation for passive myocardium: I. A new functional form, Journal of Biomechanical Engineering, Vol. 112, pp. 333-9, 1990.

[33] Simo, J. C., Taylor, R. L., Schaewe, T. J. and Miller, M. I., Quasi-incompressible finite elasticity in principal stretches: Continuum basis and numerical algorithms, Computer Methods in Applied Mechanics and Engineering, Vol. 85, pp. 273-310, 1991.

[34] Hughes, T. J. R., The Finite Element Method: Linear Static and Dynamic Finite Element Analysis, Englewood Cliffs, NJ., Prentice Hall, 1987.

[35] Fletcher, R., Practical Methods of Optimization, New Delhi, Wiley and Sons, 1989.

[36] Powell, M. J. D., "A method for nonlinear constraints in minimization problems," in *Optimization*, R. Fletcher, Ed. New York, Academic Press, 1969.

[37] Hestenes, M. R., Multiplier and gradient methods, Journal of Optimization, Theory and Applications, Vol. 4, pp. 303-320, 1969.

[38] Gonzalez, R. C. and Woods, R. E., "Digital image processing." Reading, Mass., Addison-Wesley Publishing Co., pp. 187-213, 1992.

[39] Veress, A. I., Weiss, J. A., Gullberg, G. T., Vince, D. G. and Rabbitt, R. D., Strain measurement in coronary arteries using intravascular ultrasound and deformable images, Journal of Biomechanical Engineering, Vol. 124, No. 6, pp. 734-41, 2002.

[40] Huebner, K. H., The finite element method for engineers, New York . John Wiley and Sons, Inc., 1995.

[41] Wada, H. and Metoki, T., Analysis of dynamic behavior of human middle ear using a finite-element method, Journal of the Acoustical Society of America, Vol. 92, No. 6, pp. 3157-3168, 1992.

[42] Wada, H., Ando, M., Takeuchi, M., Sugawara, H., Koike, T., Kobayashi, T., Hozawa, K., Gemma, T. and Nara, M., Vibration measurement of the tympanic membrane of guinea pig temporal bones using time-averaged speckle pattern interferometry, Journal of the Acoustical Society of America, Vol. 111, No. 5 Pt 1, pp. 2189-99, 2002.

[43] Koike, T., Wada, H. and Kobayashi, T., Modeling of the human middle ear using the finite-element method, Journal of the Acoustical Society of America, Vol. 111, No. 3, pp. 1306-17, 2002.

[44] Huber, A. M., Schwab, C., Linder, T., Stoeckli, S. J., Ferrazzini, M., Dillier, N. and Fisch, U., Evaluation of eardrum laser doppler interferometry as a diagnostic tool, Laryngoscope, Vol. 111, No. 3, pp. 501-7.

[45] Ladak, H. M. and W.R.J., F., Finite-element modeling of the normal and surgically repaired cat middle ear, Journal of the Acoustical Society of America, Vol. 100, No. 2, pp. 933-944, 1996.

[46] Maker, B., Ferencz, R. and Hallquist, J., NIKE3D A Nonlinear Implicit Three-Dimensional Finite Element Code for Solid and Structural Mechanics, UC - Lawrence Livermore National Laboratory Report, Vol. UCRL-MA-105268 rev 1, 1995.

[47] National Health and Nutrition Examination Survey (NHANES), CDC/NCHS and the American Heart Association 1996.

[48] MacIsaac, A. I., Thomas, J. D. and Topol, E. J., Toward the quiescent coronary plaque, Journal of the American Collage of Cardiology, Vol. 22, No. 4, pp. 1228-41, 1993.

[49] Richardson, P. D., Davies, M. J. and Born, G. V., Influence of plaque configuration and stress distribution on fissuring of coronary atherosclerotic plaques, Lancet, Vol. 2, No. 8669, pp. 941-4, 1989.

[50] Loree, H. M., Kamm, R. D., Stringfellow, R. G. and Lee, R. T., Effects of fibrous cap thickness on peak circumferential stress in model atherosclerotic vessels, Circulation Research, Vol. 71, No. 4, pp. 850-8, 1992.

[51] Cheng, G. C., Loree, H. M., Kamm, R. D., Fishbein, M. C. and Lee, R. T., Distribution of circumferential stress in ruptured and stable atherosclerotic lesions. A structural analysis with histopathological correlation, Circulation, Vol. 87, No. 4, pp. 1179-87, 1993.

[52] Veress, A. I., Cornhill, J. F., Herderick, E. E. and Thomas, J. D., Age-related development of atherosclerotic plaque stress: a population- based finite-element analysis, Coronary Artery Disease, Vol. 9, No. 1, pp. 13-9, 1998.

[53] Veress, A. I., Vince, D. G., Anderson, P. M., Cornhill, J. F., Herderick, E. E., Klingensmith, J. D., Kuban, B. D., Greenberg, N. L. and Thomas, J. D., Vascular mechanics of the coronary artery, Zeitschrift Fur Kardiologie, Vol. 89 Suppl 2, pp. 92-100, 2000.

[54] Loree, H. M., Tobias, B. J., Gibson, L. J., Kamm, R. D., Small, D. M. and Lee, R. T., Mechanical properties of model atherosclerotic lesion lipid pools, Arteriosclerosis and Thrombosis, Vol. 14, No. 2, pp. 230-4, 1994.

[55] Nissen, S. E., Gurley, J. C., Grines, C. L., Booth, D. C., McClure, R., Berk, M., Fischer, C. and DeMaria, A. N., Intravascular ultrasound assessment of lumen size and wall morphology in normal subjects and patients with coronary artery disease, Circulation, Vol. 84, No. 3, pp. 1087-99, 1991.

[56] Bermejo, J., Botas, J., Garcia, E., Elizaga, J., Osende, J., Soriano, J., Abeytua, M. and Delcan, J. L., Mechanisms of residual lumen stenosis after high-pressure stent implantation: a quantitative coronary angiography and intravascular ultrasound study, Circulation, Vol. 98, No. 2, pp. 112-8, 1998.

[57] Cox, R. H., Anisotropic properties of the canine carotid artery in vitro, Journal of Biomechanics, Vol. 8, No. 5, pp. 293-300, 1975.

[58] Cox, R. H., Passive mechanics and connective tissue composition of canine arteries, American Journal of Physiology, Vol. 234, No. 5, pp. H533-41, 1978.

[59] Dobrin, P. B., Biaxial anisotropy of dog carotid artery: estimation of circumferential elastic modulus, Journal of Biomechanics, Vol. 19, No. 5, pp. 351-8, 1986.

[60] Dobrin, P. B. and Doyle, J. M., Vascular smooth muscle and the anisotropy of dog carotid artery, Circulation Research, Vol. 27, No. 1, pp. 105-19, 1970.

[61] Dobrin, P. B. and Mrkvicka, R., Estimating the elastic modulus of non-atherosclerotic elastic arteries, Journal of Hypertension Suppl., Vol. 10, No. 6, pp. S7-10, 1992.

[62] Frobert, O., Gregersen, H. and Bagger, J. P., Mechanics of porcine coronary arteries ex vivo employing impedance planimetry: a new intravascular technique, Annals of Biomedical Engineering, Vol. 24, No. 1, pp. 148-55, 1996.

[63] Patel, D. J. and Janicki, J. S., Static elastic properties of the left coronary circumflex artery and the common carotid artery in dogs, Circulation Research, Vol. 27, No. 2, pp. 149-58, 1970.

[64] Patel, D. J., Janicki, J. S. and Carew, T. E., Static anisotropic elastic properties of the aorta in living dogs, Circulation Research, Vol. 25, No. 6, pp. 765-79, 1969.

[65] Salunke, N. V. and Topoleski, L. D., Biomechanics of atherosclerotic plaque, Critical Reviews in Biomedical Engineering, Vol. 25, No. 3, pp. 243-85, 1997.

[66] Weizsacker, H. W., Lambert, H. and Pascale, K., Analysis of the passive mechanical properties of rat carotid arteries, Journal of Biomechanics, Vol. 16, No. 9, pp. 703-15, 1983.

[67] Humphrey, J. D., Cardiovascular solid mechanics cells, tissues, and organs, New York, Springer-Verlag, 2002.

[68] Mazhari, R. and McCulloch, A. D., Integrative models for understanding the structural basis of regional mechanical dysfunction in ischemic myocardium, Annals of Biomedical Engineering, Vol. 28, No. 8, pp. 979-90, 2000.

[69] Kraitchman, D. L., Hillenbrand, H. B., Oznur, I., Lima, J. A., McVeigh, E. R., Zerhouni, E. A. and Bluemke, D. A., Noninvasive assessment of myocardial stunning from short-term coronary occlusion using tagged magnetic resonance imaging, Journal of Cardiovascular Magnetic Resonance, Vol. 2, No. 2, pp. 123-36, 2000.

[70] Dilsizian, V. and Bonow, R. O., Current diagnostic techniques of assessing myocardial viability in patients with hibernating and stunned myocardium, Circulation, Vol. 87, No. 1, pp. 1-20, 1993.

[71] Haas, F., Jennen, L., Heinzmann, U., Augustin, N., Wottke, M., Schwaiger, M. and Lange, R., Ischemically compromised myocardium displays different time-courses of functional recovery: correlation with morphological alterations?, European Journal of Cardiothorac Surgery, Vol. 20, No. 2, pp. 290-8, 2001.

[72] Bax, J. J., Visser, F. C., Poldermans, D., Elhendy, A., Cornel, J. H., Boersma, E., van Lingen, A., Fioretti, P. M. and Visser, C. A., Time course of functional recovery of stunned and hibernating segments after surgical revascularization, Circulation, Vol. 104, No. 12 Suppl 1, pp. I314-8, 2001.

[73] Bonow, R. O., Identification of viable myocardium, Circulation, Vol. 94, No. 11, pp. 2674-80, 1996.

[74] al-Mohammad, A., Mahy, I. R., Norton, M. Y., Hillis, G., Patel, J. C., Mikecz, P. and Walton, S., Prevalence of hibernating myocardium in patients with severely impaired ischaemic left ventricles, Heart, Vol. 80, No. 6, pp. 559-64, 1998.

[75] Ingels, N. B., Daughters, G. T., Stinson, E. B. and Alderman, E. L., Measurement of midwall myocardial dynamics in intact man by radiography of surgically implanted markers, Circulation, Vol. 52, No. 5, pp. 859-67, 1975.

[76] Ozturk, C. and McVeigh, E. R., Four-dimensional B-spline based motion analysis of tagged MR images: introduction and in vivo validation, Physics in Medicine and Biology, Vol. 45, No. 6, pp. 1683-702, 2000.

[77] Weidemann, F., Dommke, C., Bijnens, B., Claus, P., D'Hooge, J., Mertens, P., Verbeken, E., Maes, A., Van de Werf, F., De Scheerder, I., and Sutherland, G. R., Defining the transmurality of a chronic myocardial infarction by ultrasonic strain-rate imaging: implications for identifying intramural viability: an experimental study, Circulation, Vol. 107, No. 6, pp. 883-8, 2003.

[78] Weidemann, F., Eyskens, B., Jamal, F., Mertens, L., Kowalski, M., D'Hooge, J., Bijnens, B., Gewillig, M., Rademakers, F., Hatle, L., and Sutherland, G. R., Quantification of regional left and right ventricular radial and longitudinal function in healthy children using ultrasound-based strain rate and strain imaging, Journal of the American Society of Echocardiography, Vol. 15, No. 1, pp. 20-8, 2002.

[79] Weidemann, F., Jamal, F., Kowalski, M., Kukulski, T., D'Hooge, J., Bijnens, B., Hatle, L., De Scheerder, I. and Sutherland, G. R., Can strain rate and strain quantify changes in regional systolic function during dobutamine infusion, B-blockade, and atrial pacing-- implications for quantitative stress echocardiography, Journal of the American Society of Echocardiography, Vol. 15, No. 5, pp. 416-24, 2002.

[80] Weidemann, F., Kowalski, M., D'Hooge, J., Bijnens, B. and Sutherland, G. R., Doppler myocardial imaging. A new tool to assess regional inhomogeneity in cardiac function, Basic Research in Cardiology, Vol. 96, No. 6, pp. 595-605, 2001.

[81] D'Hooge, J., Konofagou, E., Jamal, F., Heimdal, A., Barrios, L., Bijnens, B., Thoen, J., Van de Werf, F., Sutherland, G. and Suetens, P., Two-dimensional ultrasonic strain rate measurement of the human heart in vivo, IEEE Transactions on Ultrasonics, Ferroelectrics, and Frequency Control., Vol. 49, No. 2, pp. 281-6, 2002.

[82] D'Hooge, J., Heimdal, A., Jamal, F., Kukulski, T., Bijnens, B., Rademakers, F., Hatle, L., Suetens, P. and Sutherland, G. R., Regional strain and strain rate measurements by cardiac ultrasound: principles, implementation and limitations, European Journal of Echocardiography, Vol. 1, No. 3, pp. 154-70, 2000.

[83] Bolster, B. D., Jr., McVeigh, E. R. and Zerhouni, E. A., Myocardial tagging in polar coordinates with use of striped tags, Radiology, Vol. 177, No. 3, pp. 769-72, 1990.

[84] Zerhouni, E. A., Parish, D. M., Rogers, W. J., Yang, A. and Shapiro, E. P., Human heart: tagging with MR imaging--a method for noninvasive assessment of myocardial motion, Radiology, Vol. 169, No. 1, pp. 59-63, 1988.

[85] Buchalter, M. B., Weiss, J. L., Rogers, W. J., Zerhouni, E. A., Weisfeldt, M. L., Beyar, R. and Shapiro, E. P., Noninvasive quantification of left ventricular rotational deformation in normal humans using magnetic resonance imaging myocardial tagging, Circulation, Vol. 81, No. 4, pp. 1236-44, 1990.

[86] McVeigh, E. R. and Atalar, E., Cardiac tagging with breath-hold cine MRI, Magnetic Resonance Medicine, Vol. 28, No. 2, pp. 318-27, 1992.

[87] McVeigh, E. R. and Zerhouni, E. A., Noninvasive measurement of transmural gradients in myocardial strain with MR imaging, Radiology, Vol. 180, No. 3, pp. 677-83, 1991.

[88] Axel, L., Goncalves, R. C. and Bloomgarden, D., Regional heart wall motion: two-dimensional analysis and functional imaging with MR imaging, Radiology, Vol. 183, No. 3, pp. 745-50, 1992.

[89] Ungacta, F. F., Davila-Roman, V. G., Moulton, M. J., Cupps, B. P., Moustakidis, P., Fishman, D. S., Actis, R., Szabo, B. A., Li, D., Kouchoukos, N. T., and Pasque, M. K., MRI-radiofrequency tissue tagging in patients with aortic insufficiency before and after operation, Annals of Thoracic Surgery, Vol. 65, No. 4, pp. 943-50, 1998.

[90] Sinusas, A. J., Papademetris, X., Constable, R. T., Dione, D. P., Slade, M. D., Shi, P. and Duncan, J. S., Quantification of 3-D regional myocardial

deformation: shape-based analysis of magnetic resonance images, American Journal Physiology Heart Circulation Physiology, Vol. 281, No. 2, pp. H698-714, 2001.

[91] Berne, R. M. and Levy, M. N., Physiology, St. Louis, MO, Mosby Year Book, 1998.

[92] Maker, B. N., Ferencz, R. M., Hallquist, J. O., Olbers, D. and Wenzel, M., NIKE3D: A nonlinear implicit three-dimensional finite element code for solid and structural mechanics Determining diffusivities from hydrographic data by inverse methods with applications to the circumpolar current Ocean Criculation Models: Combining Data and Dynamics, presented at Lawrence Livermore National Laboratory Technical Report, Dordrech, 1990.

[93] Ramani, K., Judd, R. M., Holly, T. A., Parrish, T. B., Rigolin, V. H., Parker, M. A., Callahan, C., Fitzgerald, S. W., Bonow, R. O. and Klocke, F. J., Contrast magnetic resonance imaging in the assessment of myocardial viability in patients with stable coronary artery disease and left ventricular dysfunction, Circulation, Vol. 98, No. 24, pp. 2687-94, 1998.

[94] Kim, R. J., Wu, E., Rafael, A., Chen, E. L., Parker, M. A., Simonetti, O., Klocke, F. J., Bonow, R. O. and Judd, R. M., The use of contrast-enhanced magnetic resonance imaging to identify reversible myocardial dysfunction, New England Journal of Medicine, Vol. 343, No. 20, pp. 1445-53, 2000.

[95] Szolar, D. H., Saeed, M., Wendland, M. F., Sakuma, H., Roberts, T. P., Stiskal, M. A., Derugin, N. and Higgins, C. B., MR imaging characterization of postischemic myocardial dysfunction ("stunned

myocardium"): relationship between functional and perfusion abnormalities, Journal of Magnetic Resonance Imaging, Vol. 6, No. 4, pp. 615-24, 1996.

[96] Wu, E., Judd, R. M., Vargas, J. D., Klocke, F. J., Bonow, R. O. and Kim, R. J., Visualisation of presence, location, and transmural extent of healed Q-wave and non-Q-wave myocardial infarction, Lancet, Vol. 357, No. 9249, pp. 21-8, 2001.

[97] Gerber, B. L., Garot, J., Bluemke, D. A., Wu, K. C. and Lima, J. A., Accuracy of contrast-enhanced magnetic resonance imaging in predicting improvement of regional myocardial function in patients after acute myocardial infarction, Circulation, Vol. 106, No. 9, pp. 1083-9, 2002.

[98] Choi, K. M., Kim, R. J., Gubernikoff, G., Vargas, J. D., Parker, M. and Judd, R. M., Transmural extent of acute myocardial infarction predicts long-term improvement in contractile function, Circulation, Vol. 104, No. 10, pp. 1101-7, 2001.

[99] Costa, K. D., Hunter, P. J., Wayne, J. S., Waldman, L. K., Guccione, J. M. and McCulloch, A. D., A three-dimensional finite element method for large elastic deformations of ventricular myocardium: II--Prolate spheroidal coordinates, Journal of Biomechanical Engineering, Vol. 118, No. 4, pp. 464-72, 1996.

[100] Costa, K. D., Hunter, P. J., Rogers, J. M., Guccione, J. M., Waldman, L. K. and McCulloch, A. D., A three-dimensional finite element method for large elastic deformations of ventricular myocardium: I--Cylindrical and spherical polar coordinates, Journal of Biomechanical Engineering, Vol. 118, No. 4, pp. 452-63, 1996.

[101] Guccione, J. M., McCulloch, A. D. and Waldman, L. K., Passive material properties of intact ventricular myocardium determined from a cylindrical model, Journal of Biomechanical Engineering, Vol. 113, No. 1, pp. 42-55, 1991.

[102] Needleman, A., Rabinowitz, S. A., Bogen, D. K. and McMahon, T. A., A finite element model of the infarcted left ventricle, J Biomech, Vol. 16, No. 1, pp. 45-58, 1983.

[103] Vito, R. P. and Hickey, J., The mechanical properties of soft tissues--II: the elastic response of arterial segments, Journal of Biomechanics, Vol. 13, No. 11, pp. 951-7, 1980.

[104] Vito, R. P., The mechanical properties of soft tissues--I: a mechanical system for bi-axial testing, Journal of Biomechanics, Vol. 13, No. 11, pp. 947-50, 1980.

[105] Allaire, P. E., Thacker, J. G., Edlich, R. F., Rodeheaver, G. J. and Edgerton, M. T., Finite deformation theory for in vivo human skin, Journal of Bioengineering, Vol. 1, No. 3, pp. 239-49, 1977.

[106] Gardiner, J. C., Weiss, J. A. and Rosenberg, T. D., Strain in the human medial collateral ligament during valgus loading of the knee, Clinical Orthopaedics, No. 391, pp. 266-74, 2001.

[107] Gardiner, J. C. and Weiss, J. A., Effects of flexion angle and valgus rotation on stresses in the human medial collateral ligament Proc ASME Bioengineering Conference Vol. BED-35 No., pp. 27-28 1997

[108] Quapp, K. M. and Weiss, J. A., Material characterization of human medial collateral ligament, Journal of Biomechanical Engineering, Vol. 120, No. 6, pp. 757-63, 1998.

[109] Weiss, J. A., Gardiner, J. C. and Quapp, K. M., Material models for the study of soft tissue mechanics, Proceeding of the International Conference on Pelvic and Lower Extremity Injuries, December 4-6, pp. 249-261, 1995.

[110] Johnson, H. J. and Christensen, G. E., Consistent landmark and intensity-based image registration, IEEE Transactions on Medical Imaging, Vol. 21, No. 5, pp. 450-461, 2002.

[111] Christensen, G. E. and Johnson, H. J., Consistent image registration, IEEE Transactions on Medical Imaging, Vol. 20, No. 7, pp. 568-582, 2001.

[112] Maintz, J. B. and Viergever, M. A., A survey of medical image registration, Medical Image Analysis, Vol. 2, No. 1, pp. 1-36, 1998.